Dual-Frequency Wind-Driven Mixed Rossby–Gravity Waves in the Equatorial Indian Ocean

MOTOKI NAGURA[a] AND MICHAEL J. MCPHADEN[b]

[a] *Japan Agency for Marine-Earth Science and Technology, Kanagawa, Japan*
[b] *National Oceanic and Atmospheric Administration/Pacific Marine Environmental Laboratory, Seattle, Washington*

ABSTRACT: Frequency spectra of in situ meridional velocity measurements in the central equatorial Indian Ocean show two distinct peaks at "quasi biweekly" periods of 10–30 days. One is near the surface at frequencies of 0.06–0.1 cpd (periods of 10–17 days) and the other is in the pycnocline (~100-m depth) at lower frequencies of 0.04–0.06 cpd (periods 17–25 days). Analysis of a wind-forced ocean general circulation model shows that variability in the two frequency bands represents wind-driven mixed Rossby–gravity waves. The waves share a similar horizontal structure, but the meridional scale of lower-frequency variability is about one-half of that of higher-frequency variations. Higher-frequency variability has its largest amplitude in the eastern basin while the lower-frequency variability has its largest amplitude in the central basin. The vertical wavelength of lower-frequency variability is smaller by a factor of 3–4 than that of higher-frequency variability. These results are consistent with expectations from linear mixed Rossby–gravity wave theory. Numerical simulations show that the primary driver of these waves is surface wind forcing in the central and eastern Indian Ocean and that dynamical instability does not play a major role in their generation.

SIGNIFICANCE STATEMENT: Spectra of meridional velocity in the central equatorial Indian Ocean from in situ measurements show two distinct peaks in the biweekly period band with different spatial structures. This study uses an ocean general circulation model to show that variability in these two bands is driven by surface winds that are themselves spatially structured. The variability in both period bands is consistent with linear mixed Rossby–gravity wave theory, but the spatial structures, including meridional trapping scale, vertical wavelength, and zonal distribution of energy, are very different.

KEYWORDS: Ocean; Indian Ocean; Oceanic waves; Intraseasonal variability

1. Introduction

Intraseasonal variability in cross-equatorial meridional velocity is very prominent in the Indian Ocean (Masumoto et al. 2005; Nagura et al. 2014; Ogata et al. 2008; Reppin et al. 1999; Pujiana and McPhaden 2021, hereinafter PM21). This variability has been attributed to mixed Rossby–gravity waves driven by surface winds (Arzeno et al. 2020; Miyama et al. 2006; PM21; Sengupta et al. 2004). The atmosphere has variability at periods from 10 to 30 days (referred to as the quasi-biweekly mode), which is the manifestation of the first meridional mode atmospheric Rossby wave (Chen and Chen 1993, 1995; Kikuchi and Wang 2009; Kiladis and Wheeler 1995; Krishnamurti and Ardanuy 1980). The first meridional mode of atmospheric Rossby waves is meridionally antisymmetric owing to the ambient potential vorticity field (Chatterjee and Goswami 2004), resulting in cross-equatorial winds and the excitation of oceanic mixed Rossby–gravity waves. Mixed Rossby–gravity waves propagate vertically through the pycnocline (Miyama et al. 2006; Ogata et al. 2008) and are of climatic importance because they generate residual heating and mean upwelling along the equator (Nagura et al. 2014; Ogata et al. 2017; Smyth et al. 2015), potentially driving abyssal mixing near the ocean bottom

(Holmes et al. 2016; Delorme and Thomas 2019). Mixed Rossby–gravity waves with short zonal wavelengths (~1000 km) also generate mean zonal jets near the equator below the pycnocline (Ascani et al. 2010; d'Orgeville et al. 2007; Hua et al. 2008; Ménesguen et al. 2009).

Previous studies describe the spatial structure, frequency, zonal wavelength and other wave properties of mixed Rossby–gravity waves in the central and eastern Indian Ocean using in situ observations, satellite measurements and model results (Arzeno et al. 2020; Nagura et al. 2014; Ogata et al. 2008; PM21; Sengupta et al. 2004; Smyth et al. 2015). The results of these studies show a typical period of 10–25 days and a typical zonal wavelength of about 4000 km.

PM21 further pointed out that mixed Rossby–gravity waves in the equatorial Indian Ocean are not monochromatic but are energetic in two distinct frequency bands. They analyzed in situ meridional velocity measurements from an array of acoustic Doppler current profilers (ADCPs) centered at 0°, 80.5°E and found two spectral peaks, one at periods of 10–15 days with the energy highest in the upper 100 m and the other at periods of 15–25 days with energy highest in the thermocline at depths of 100–150 m. Ogata et al. (2008) also used in situ observations and reported that the peak of the spectrum of meridional velocity is at periods of 12–18 days at 50-m depth but at 20–40-day periods at 250-m depth. Both PM21 and Ogata et al. (2008) focused their analyses on the

higher of the two frequency bands, leaving the examination of lower-frequency variability for future work. Masumoto et al. (2005) also reported higher (lower) frequency variability above (in the lower part of) the thermocline basing their analysis on in situ observations.

The energy source for these waves has been a matter of debate. David et al. (2011), for example, computed the baroclinic and barotropic energy conversion rate using satellite observations and compared the result between the years when low-frequency mixed Rossby–gravity waves are large in amplitude and those when waves are weak. They proposed a hypothesis that the dynamical instability of the westward south equatorial current and the eastward southwest monsoon current contributes to the generation of lower-frequency mixed Rossby–gravity waves energy in the central equatorial Indian Ocean.

This study examines variability in both the higher- and lower-frequency quasi-biweekly period bands and describes the difference between them using an ocean general circulation model (OGCM). Hereinafter, we refer to frequencies of 0.06–0.1 cpd (10–17 days in period) as high frequency (HF) and those of 0.04–0.06 cpd (17–25 days in period) as low frequency (LF). The paper is organized as follows. We introduce the observations and the OGCM used in this study in section 2. Section 3 describes the results of statistical analysis and numerical experiments. Section 4 summarizes the main results.

2. Data and model

a. Observations

In situ measurements of horizontal velocity were obtained from an array of upward-looking moored ADCPs centered at 0°, 80.5°E (marked by the star in Fig. 1a) embedded in the Research Moored Array for African–Asian–Australian Monsoon Analysis and Prediction (RAMA; McPhaden et al. 2009, 2015). The ADCPs were mounted in subsurface spherical floats with a nominal target depth of 250–300 m (PM21). Data are available at daily resolution in time and 5-m resolution in the vertical direction. The shallowest useful data are typically found at a depth of 30–40 m because of acoustic interference from backscatter off the ocean surface. We used daily averages at 0°, 80.5°E and filled data temporal gaps using observations from ADCP moorings at 0.75°N and 0.75°S along 80.5°E according to the method of Johnson and McPhaden (1993) as described in McPhaden et al. (2015) and Wang et al. (2015). The data period spanned from 16 August 2008 to 6 February 2016.

Surface wind stress data were obtained from the Japanese 55-year atmospheric reanalysis, which is referred to as JRA55-do (Tsujino et al. 2018). The JRA55-do data are available on a 55-km latitude–longitude grid with a time interval of 3 h. Monthly averages of temperature and salinity data were obtained from a dataset provided by Roemmich and Gilson (2009), which was constructed by objectively gridding Argo float observations on a 1° × 1° grid at 58 levels in the upper 2000 m.
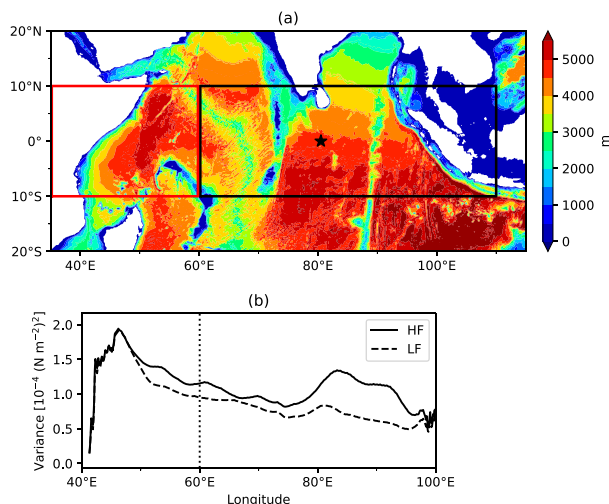

FIG. 1. (a) The depth of the ocean bottom of our OGCM (color shades). The central and eastern Indian Ocean region (10°S–10°N, 60°–110°E) is shown by the black-outlined box. The western Indian Ocean region (10°S–10°N, 35°–60°E) is shown by the red-outlined box. The location of the RAMA mooring buoy (0°, 80.5°E) is shown by the black star. (b) Variance-preserving spectra of meridional wind stress in 2°S–2°N averaged over the HF (solid line) and LF (dashed line) bands as a function of longitude. The HF and LF bands are defined as frequencies of 0.06–0.1 cpd (10–17 days in period) and those of 0.04–0.06 cpd (17–25 days in period), respectively. The vertical dotted line marks the boundary between the two regions.

b. Model

1) MODEL CONFIGURATION

The model used in this study is the OGCM for the Earth Simulator (OFES; Masumoto et al. 2004; Sasaki et al. 2020), which is constructed from the Modular Ocean Model, version 3 (Pacanowski and Griffies 2000). We set our model domain to be 20°S–20°N and 35°–115°E, which is bounded by solid walls (Fig. 1a). The horizontal grid is 0.1° in longitude and latitude. The model has 105 vertical levels. The vertical grid intervals are less than 10 m in the upper 205 m and less than 20 m in the upper 600 m, which are small enough to resolve variability examined in this study. The bottom topography (Fig. 1a) is generated from ETOPO1 (Amante and Eakins 2009) using the method of partial bottom cells (Adcroft et al. 1997). Vertical mixing is parameterized following Noh and Kim (1999). Biharmonic horizontal mixing is adopted with coefficients for momentum and tracers of 27×10^9 and 9×10^9 m^4 s^{-1}, respectively.

The model was forced by 3-hourly averages of meteorological variables (surface winds, air temperature and humidity at 10-m height, air pressure at the sea level, rainfall, and downward shortwave and longwave radiation) obtained from JRA55-do. Momentum, heat, and freshwater fluxes were computed with the bulk formulas of Large and Yeager (2004). Monthly climatological freshwater flux due to river runoff was obtained from Coordinated Ocean-Ice Reference Experiments version 2 (Dai et al. 2009) and added to the freshwater forcing. In addition, the
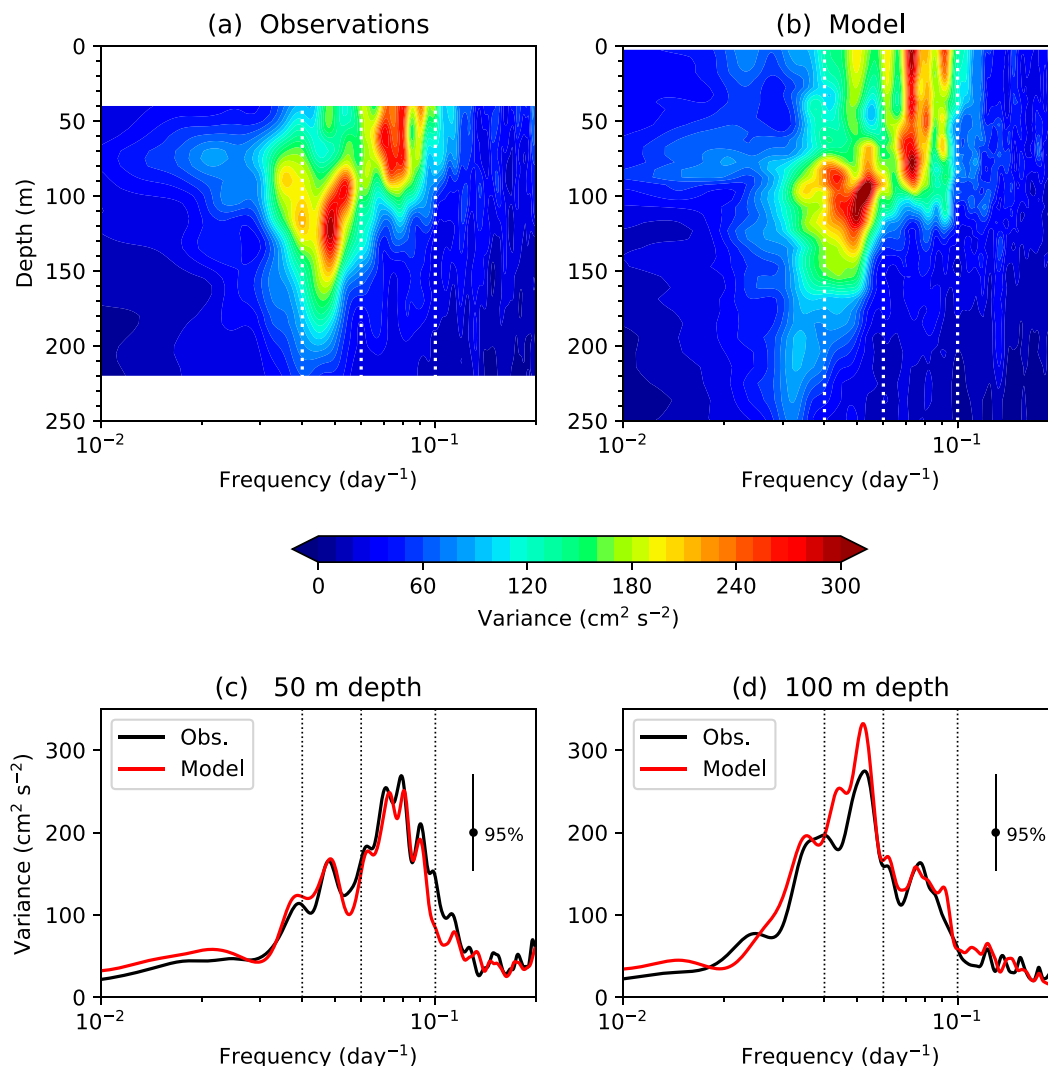
FIG. 2. Variance-preserving spectra of meridional velocity at 0°, 80.5°E as a function of frequency and depth obtained from (a) ADCP observations and (b) the control run of the model. Also shown are spectra of meridional velocity at (c) 50- and (d) 100-m depth for ADCP observations (black line) and the control run of the model (red line). The error bar is for the 95% confidence level. Frequencies of 0.04, 0.06, and 0.1 cpd (periods of 25, 17, and 10 days) are marked by the vertical dotted lines.

model sea surface salinity was restored to the *World Ocean Atlas 2013* (*WOA13*; Locarnini et al. 2013; Zweng et al. 2013) with a damping time scale of 15 days. The model temperature and salinity near the northern and southern walls were restored toward *WOA13* with a time scale of 1 day to prevent waves from propagating along the artificial boundaries.

We first spun up the model for 10 years using repeated 1999 surface meteorological forcing and then ran the model from 2000 to 2016. Initial conditions were obtained from *WOA13*. This model run is referred to as the control run. We used daily averages of the model output for the period from 16 August 2008 to 6 February 2016 for our analysis. During this period, the model solution was validated by comparing with ADCP observations (next section).

2) COMPARISON WITH OBSERVATIONS

As PM21 pointed out, the spectra of meridional velocity observed at 0°, 80.5°E peak in two distinct frequency bands. In the HF band, the spectral power is elevated in the upper 100 m, whereas it is largest at depths from 80 to 170 m in the LF band (Fig. 2a). Our study was motivated by the desire to understand this unusual structure.

The spectra of simulated meridional velocity also show distinct energy peaks, one of which is in the HF band in the upper 100 m and the other in the LF band in 70–150-m depths (Fig. 2b). Qualitatively, the model and observations agree well in magnitude and spatial structure, with only minor discrepancies. For example, energy in the HF band at 50-m depth is slightly higher in observations than in the
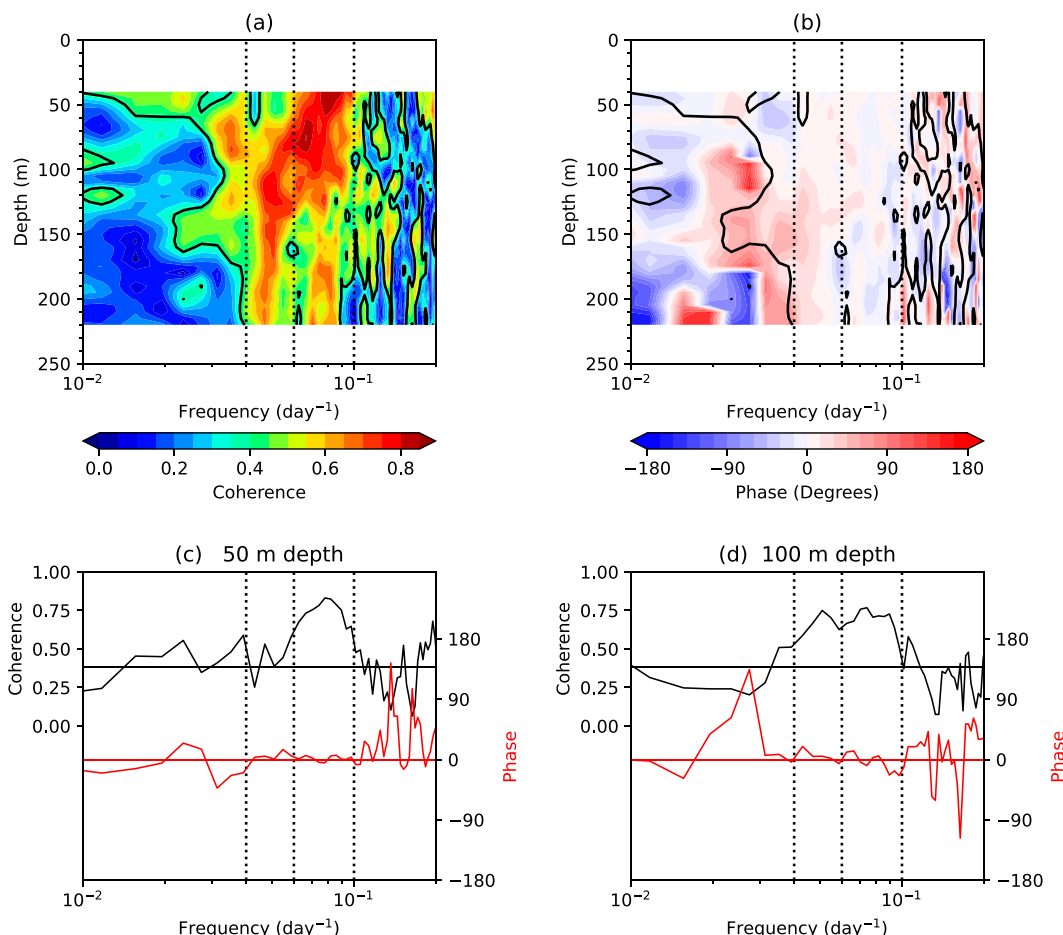
FIG. 3. (a) Coherence and (b) phase between meridional velocity at 0°, 80.5°E obtained from ADCP observations and the control run of the model as a function of frequency and depth. The solid lines in (a) illustrate the area where coherence exceeds the 95% confidence level. Also shown are coherence (black line) and phase (red line) at (c) 50- and (d) 100-m depth. The black horizontal line shows the 95% confidence level for coherence. The red horizontal line is for a phase of 0°. The vertical dotted lines mark frequencies of 0.04, 0.06, and 0.1 cpd (periods of 25, 17, and 10 days).

model (Fig. 2c). Energy in the LF band peaks at about 100-m depth, which is higher in the model than in observations (Fig. 2d). These differences are statistically insignificant and may be due to minor differences in mean stratification between the observations and model and/or detailed differences in wind forcing.

Observed and simulated meridional velocity is highly coherent in the upper 200 m in both the HF and LF bands where spectral energy is high (Figs. 3a,c,d). Coherence in the HF and LF bands is significant at the 95% confidence level and the phase difference is close to zero. Coherence is not significant outside of the HF and LF bands, possibly because spectral energy is low and the signal-to-noise ratio is small. The result shows that the model is well validated in comparison with the in situ observations.

Figure 4 compares the stratification between Argo float observations and the control run of our model. The observed mean buoyancy frequency squared (N^2) at 0°, 80°E is largest at about 100 m (Fig. 4a, black line), which is the pycnocline.

The observed pycnocline is centered at about 100-m depth along the equator (Fig. 4b) between 3°N and 3°S (Fig. 4d). It shoals to about 50-m depth south of 3°S. The N^2 in the pycnocline is largest in the east (Fig. 4b) and near the equator (Fig. 4d). The pycnocline deepens in May–July and November–January (Fig. 4f), which is roughly in phase with sea surface height variability related to the semiannual Wyrtki jet (Nagura and McPhaden 2010), i.e., the deep pycnocline coincides with elevated sea surface and vice versa. The N^2 in the pycnocline is large from May to August and relatively small in other months. The model is able to simulate the depth of the peak (Fig. 4a, red line), the zonal and (Fig. 4c) meridional (Fig. 4e) structures, and seasonal variability (Fig. 4g) of N^2, although it tends to overestimate the peak magnitude of N^2. The model is also able to roughly simulate the structure of the stratification in the sensitivity experiments (figure not shown). Thus, except for minor, quantitative differences, the model simulates the stratification very well for our purposes.
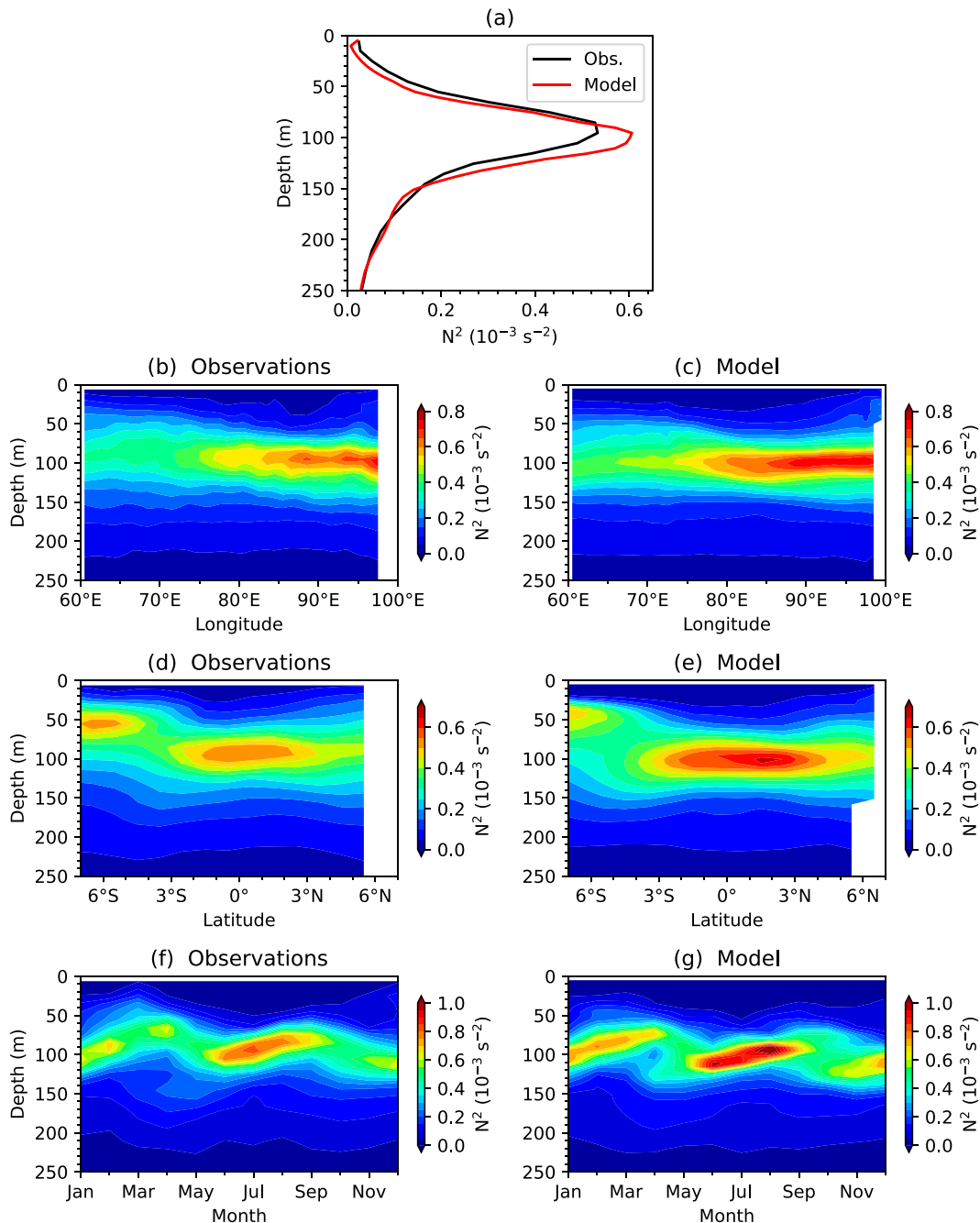
FIG. 4. Comparison of buoyancy frequency squared (N^2) between (left) Roemmich and Gilson's (2009) Argo float observations and (right) the control run of the model: The mean N^2 (a) at 0°, 80°E as a function of depth, (b),(c) along the equator as a function of longitude and depth, and (d),(e) along 80°E as a function of latitude and depth. (f),(g) Monthly climatologies of N^2 at 0°, 80°E as a function of month and depth. The black and red lines in (a) are for observations and model results, respectively. The mean and monthly climatologies were calculated for the period from August 2008 to February 2016. Model results are averaged over 1° × 1° boxes for consistency with Roemmich and Gilson's dataset.

3) SENSITIVITY EXPERIMENTS

To check the response of the ocean to surface wind forcing in the HF and LF bands, we conducted sensitivity experiments using temporally filtered surface wind stress. Surface wind stress data were obtained from JRA55-do using Large and Yeager's (2004) bulk formula. The initial conditions for the sensitivity experiments were obtained from the control run at the end of 2007. The model was then run from 2008 to

2016, with results examined from 16 August 2008 to 6 February 2016. Surface buoyancy fluxes were computed from 3-hourly averages of JRA55-do surface meteorological variables as in the control run.

In the sensitivity experiments, the model was driven by the sum of band passed intraseasonal (referred to as τ_{intr}) and background (τ_{back}) surface wind stress. The τ_{intr} represents variability in surface wind stress in the HF or LF band obtained from a Butterworth bandpass filter. The τ_{back} was computed using a low-pass Butterworth filter with the cutoff frequency at 0.01 cpd (100 days in period). The τ_{back} includes the temporal mean, which is necessary to maintain the mean pycnocline. Intraseasonal variability in surface meridional wind stress shows spectral peaks in two distinct regions along the equator, that is, the central and eastern regions between 80° and 90°E and the region near the western boundary west of about 60°E (Fig. 1b). The former will act as regional wind forcing on waves in the central equatorial Indian Ocean and the latter as a remote forcing. In the first set of experiments, we set τ_{intr} to zero outside of the central and eastern equatorial Indian Ocean (10°S–10°N and 60°–110°E; black-outlined box in Fig. 1a) to check the impact of $\tau_{intr} + \tau_{back}$ regional wind forcing and τ_{back} elsewhere. We refer to the experiment in which HF (LF) variability is used for τ_{intr} as HF-TAU-CE (LF-TAU-CE), where "CE" denotes "central and eastern." In the second set of experiments, we set τ_{intr} to zero outside of the western equatorial Indian Ocean (10°S–10°N, 35°–60°E; red-outlined box in Fig. 1a) to determine the impact of wind forcing in the western basin. These experiments are referred to as HF-TAU-W and LF-TAU-W experiments ("W" is for "western"). The structure and zonal phase speed of surface wind stress in the sensitivity experiments are essentially the same as those in the control run which indicates that our filtering method does not significantly distort the surface wind field. In this study, zonal phase speed and its uncertainty are estimated by the method of Barron et al. (2009), which calculates the standard deviation of the target variable along straight lines in the longitude–time section with various slopes and selects the one for which the standard deviation is minimized.

Previous studies pointed out that the mean currents in the central equatorial Indian Ocean (David et al. 2011) and those in the western Indian Ocean (Chatterjee et al. 2013; Kindle and Thompson 1989; Woodberry et al. 1989) are dynamically unstable and possibly contribute to the generation of mixed Rossby–gravity waves in the central and eastern Indian Ocean in a period band similar to that for wind forced mixed Rossby–gravity waves. To check these possibilities, we forced the model with only τ_{back}, which is referred to as BACK-TAU experiment.

3. Results

a. Statistical analysis

In this section, we first describe horizontal and vertical structures of the wave variability. Second, we compare zonal and vertical wavenumbers estimated from model results with the dispersion relation of free, mixed Rossby–gravity waves in an ocean with a mean state at rest. Third, we describe the surface wind forcing on intraseasonal time scales.

1) SPATIAL STRUCTURES

Spectral power along 80.5°E shows that HF variability in meridional velocity is largest in magnitude in the upper 30 m between 3°N and 3°S and that energy higher than 100 cm² s⁻² penetrates into ~120-m depth (Fig. 5a). The off-equatorial peaks near the surface suggest the contribution from wave modes other than mixed Rossby–gravity waves, as mixed Rossby–gravity waves have the largest variance in meridional velocity on the equator (e.g., PM21). The longitude–depth section along the equator shows elevated HF variability in the upper 120 m with peak magnitudes between 48°–54°E and 82°–96°E (Fig. 5b). In contrast, the spectral power of meridional velocity averaged over the LF band shows a different spatial distribution. In latitude and depth, variance peaks near the equator and at about 100-m depth (Fig. 5c). Elevated energy is meridionally narrower in the LF band than in the HF band. Power averaged over the LF band shows a zonally elongated peak at about 100-m depth from 60° to 95°E (Fig. 5d). Power in this frequency band is also large in the upper 30 m between 60° and 70°E and in the upper 130 m between the western boundary and about 60°E. The variance west of 70°E exceeds 300 cm² s⁻² with a maximum of about 770 cm² s⁻² near 50°E. A kink at about 73°E is likely a result of a perturbation caused by the Maldive Islands as reported in other studies of equatorial wave propagation in the Indian Ocean (Chen et al. 2020; Han et al. 1999; Miyama et al. 2006; Nagura and Masumoto 2015; Strutton et al. 2015; Yoon 1981).

Horizontal and vertical structures were estimated by regressing horizontal velocity onto HF and LF bandpassed meridional velocity at 0°, 80.5°E. Considering that meridional velocity peaks in magnitude at different depths depending on frequency (Fig. 2), we used index time series at 52.5-m depth for HF variability and at 102.5-m depth for LF variability. Details of the regression analysis are described in the appendix. As described there, essentially the same results are obtained if we use index time series of meridional velocity at slightly different longitudes or depths as those specified above.

The horizontal maps of regressed velocity show that HF variability is characterized by cross-equatorial velocity and circulating pattern between 6°N and 6°S (Figs. 6a,c,e), which resembles the theoretical structure of mixed Rossby–gravity waves as pointed out by Sengupta et al. (2004), Ogata et al. (2008), and PM21. The pattern propagates to the west (Fig. 7a) with a phase speed of −3.8 m s⁻¹ (the range of uncertainty is from −3.6 to −3.9 m s⁻¹; parameter values are summarized in Table 1). Our estimate roughly agrees with those obtained from previous observational studies but is slightly larger than theirs. PM21 examined in situ velocity measurements at several points along the equator and estimated the zonal phase speed for HF variability as −2.9 ± 0.3 m s⁻¹. Arzeno et al. (2020) examined HF variability in satellite altimetry and obtained results from −2.33 to −2.79 m s⁻¹ and from −2.48 to −3.8 m s⁻¹ using autocorrelations and cross-spectral analysis, respectively.
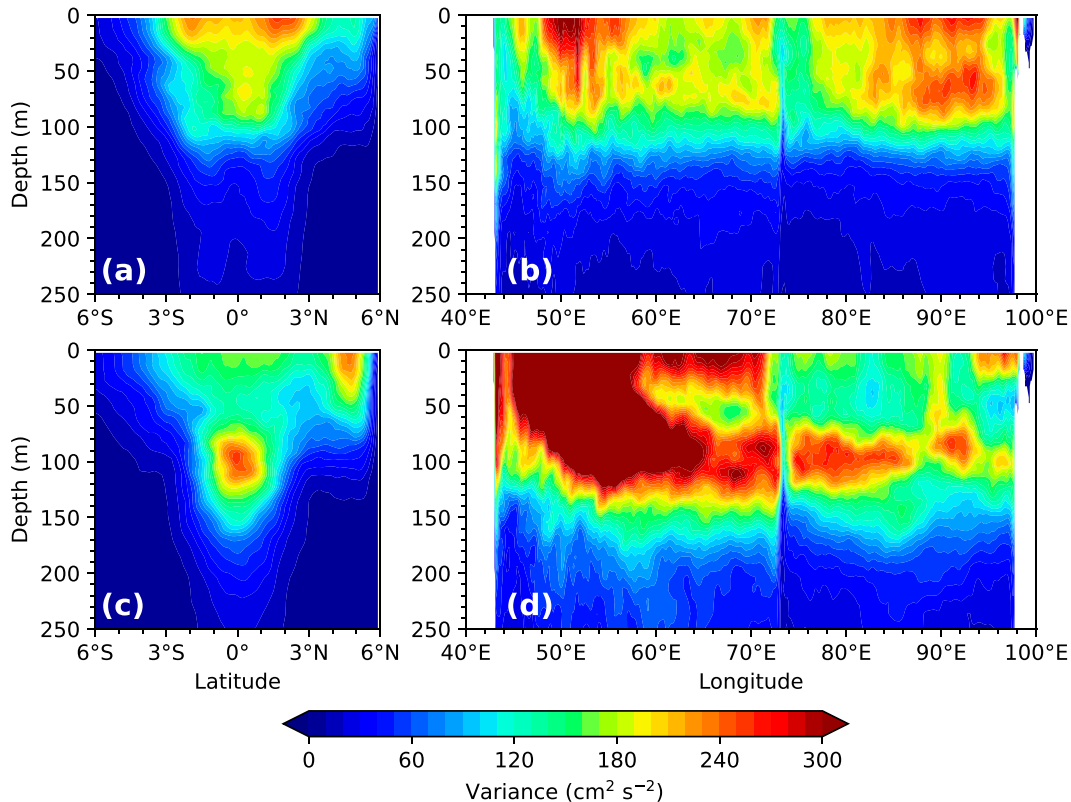
FIG. 5. Spectral power of meridional velocity averaged over the HF band (0.06–0.1 cpd; 10–17 days in period) (a) along 80.5°E and (b) along the equator. (c),(d) As in (a) and (b), but for the LF band (0.04–0.06 cpd; 17–25 days in period). Note that the color scale, which is the same as that in Figs. 2a and 2b, saturates above 300 cm² s⁻².

LF variability also shows a similar circulation pattern, but it is meridionally confined to 3°N and 3°S (Figs. 6b,d,f). LF variability propagates to the west with a phase speed of -2.7 m s⁻¹ (the range of uncertainty is from -2.6 to -2.9 m s⁻¹; Fig. 7b). The results show both HF and LF variability has a spatial pattern that is similar to mixed Rossby–gravity waves but that the LF variability is meridionally narrower than HF variability.

Regressed meridional velocity shows that HF variability is trapped near the surface where it tends to be uniform vertically in the upper 100 m (Figs. 8a,c,e). Below that, as shown by PM21, the phase propagates upward (Fig. 8g), indicating downward energy propagation (McCreary 1984). In the LF band, northward and southward velocity is vertically stacked (Figs. 8b,d,f) with shorter vertical wavelengths relative to HF variability. Regressed meridional velocity in the LF band also tends to tilt upward to the east, but its inclination is larger relative to HF variability. The upward phase propagation in the LF band (Fig. 8h) is also consistent with downward energy propagation.

2) WAVELENGTH AND DISPERSION RELATION

We estimated the zonal wavelength using coherence and phase between each longitude and 80.5°E from model meridional velocity along the equator. The results were averaged over the HF band using an index time series at 52.5-m depth (Figs. 9a,e) where the amplitude of HF variability is large

(Figs. 2a,b). The zonal wavelength was estimated by fitting a straight line to the phase in the region where coherence exceeds the 99.5% confidence level and phase changes at an approximately constant rate. For LF variability, coherence and phase were computed similarly but using a meridional velocity index time series at 102.5-m depth (Figs. 9b,f). We estimated the vertical wavelength by applying coherence analysis to the vertical profiles of meridional velocity at 0°, 80.5°E and fitting a straight line to the phase in the vertical direction (Figs. 9c,d,g,h). Wavelength error was computed as the 99% confidence level of the straight line fit. The results are essentially the same if we use meridional velocity at slightly different longitude or depth as the index time series (see the appendix).

Coherence is high between about 70° and 95°E for HF variability and between 75° and 85°E for LF variability (Figs. 9a,b). The estimated zonal wavelength is about 5242 ± 368 km for HF variability and 4364 ± 1335 km for LF variability. The zonal width of positive values of regressed meridional velocity at 52.5 m in Fig. 8c is about 2090 km, which roughly agrees with half the zonal wavelength estimated from coherence analysis for HF variability, 2621 km. The zonal width of positive values at 102.5-m depth in Fig. 8d is about 2420 km, which is also comparable to one-half of the wavelength estimated from coherence analysis for LF variability, 2182 km. The equatorial Indian Ocean is about 6000 km wide, so based on these results the
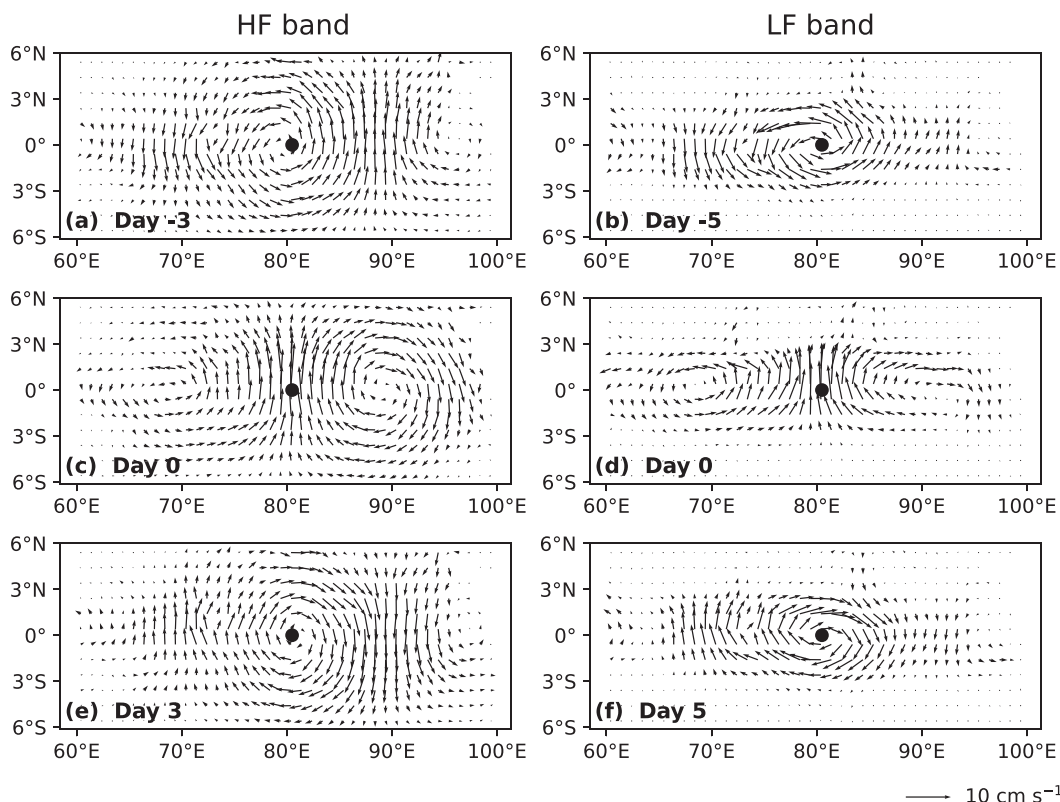
FIG. 6. (a),(c),(e) Maps of horizontal velocity at 52.5-m depth in the HF (0.06–0.1 cpd; 10–17 days in period) band regressed onto meridional velocity at 0°, 80.5°E at the same depth. (b),(d),(f) As in (a), (c), and (e), but for velocity at 102.5-m depth in the LF (0.04–0.06 cpd; 17–25 days in period) band. The index time series for the regression analysis is normalized by its standard deviation. The black dot shows the location of the index time series. The results for HF variability are shown at days −3, 0, and 3, which are apart by one-quarter of a cycle at 0.08 cpd (~12 days in period). Similarly, the results for LF variability are shown every 5 days, which corresponds to one-quarter of a cycle in this frequency band.

mixed Rossby–gravity waves are basin scale, as PM21 noted. PM21 estimated a zonal wavelength of HF variability as 3430 ± 550 km using in situ velocity measurements; Arzeno et al. (2020) obtained 3700 ± 400 km from satellite altimetry. Our estimate is comparable to theirs, although ours is slightly larger. This is consistent with the fact that our estimate of zonal phase speed tends to be larger than those from previous studies [section 3a(1)]. The reason for this discrepancy is unclear, but the sensitivity of our model results to the details of the imposed atmospheric forcing data is a possible candidate.

In the vertical direction, high coherence is found in the upper 100 m for HF variability and between 60- and 150-m depths for LF variability (Figs. 9c,d). For LF variability, phase changes are faster at depths from 50 to 140 m but slower below 140-m depth. LF variability is large in 50–140-m depths (Fig. 2b), so we fit a straight line to the phase in this depth range. The estimated vertical wavelength is about 1053 ± 313 m for HF variability and about 297 ± 32 m for LF variability. PM21 estimated a vertical wavelength for HF variability as 760 ± 150 m using in situ velocity observations, which is indistinguishable from our estimate within the range of error.

The dispersion relation obtained from the shallow water equation for mixed Rossby–gravity waves is written as $k = \omega/c - \beta/\omega$, where k is zonal wavenumber, ω is frequency, β is the meridional gradient of the Coriolis coefficient, and c is gravity wave phase speed for a specific vertical mode. We computed vertical modes from the stratification of our model and projected regressed meridional velocity in Fig. 8 onto these vertical modes, which form a complete set for representing the variability. The stratification was obtained from model N^2 averaged over 3°S–3°N, 60°–100°E and the analysis period. The vertical modes were calculated by solving the equation $\partial_z[(N^2)^{-1}\partial_z\psi_n] = -c_n^{-2}\psi_n$, where ψ_n is the nth vertical mode function as a function of depth, and c_n is c for the nth mode. This formulation assumes that the background state is at rest. We also computed dynamical modes including the effect of zonal mean currents using the method of Proehl (1998), but the results were almost the same as those obtained assuming a state of rest.

The result shows that the first three modes are the major contributor to HF variability (Fig. 10a). The significant contributions from lowest vertical modes are consistent with the large vertical wavelength of the HF variability. The superposition of
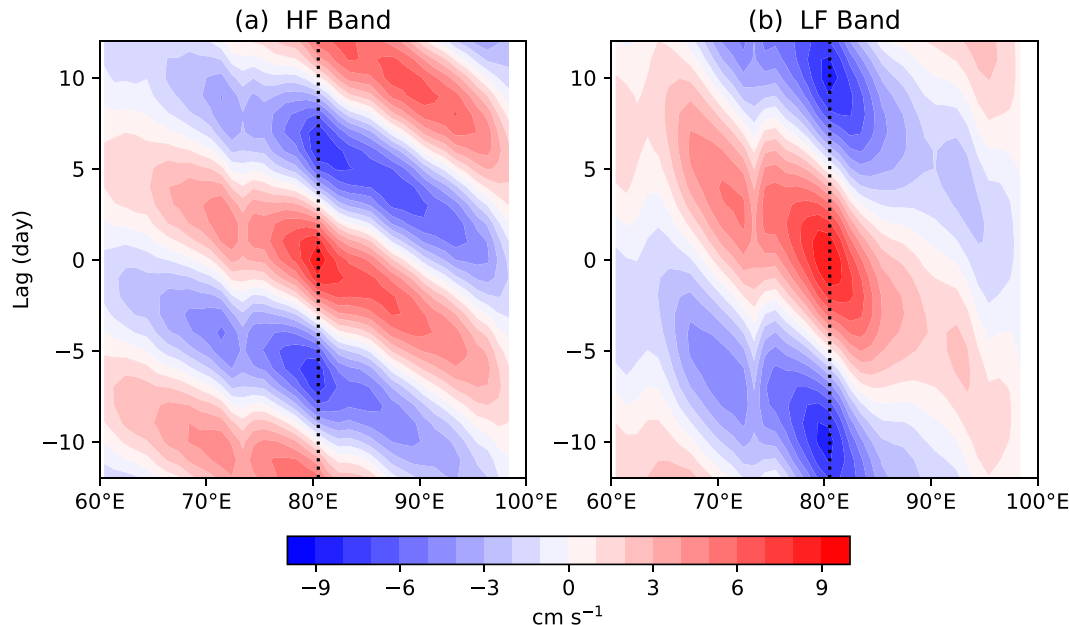
FIG. 7. Meridional velocity along the equator regressed onto meridional velocity at 0°, 80.5°E for (a) HF (0.06–0.1 cpd; 10–17 days in period) variability at 52.5-m depth and (b) LF (0.04–0.06 cpd; 17–25 days in period) variability at 102.5-m depth. The index time series is normalized by its standard deviation. The location of the index time series is shown by the dotted line.

these dominant modes manifests itself in the tendency for vertical propagation of HF variability (Fig. 8g) consistent with previous work that shows how the sum of phase locked vertical modes can result in vertical energy propagation in the equatorial ocean (e.g., Rothstein et al. 1985).

For a given frequency, c can be calculated from k using the dispersion relation. We used $k = -1.20 \times 10^{-6}$ m^{-1} estimated from coherence analysis for HF variability and $\omega = 0.08$ cpd to obtain $c = 2.13 \pm 0.07$ m s^{-1}. This estimate falls between the phase speed of first and second baroclinic mode gravity waves (2.94 and 1.86 m s^{-1}, respectively) consistent with the above analysis. PM21 made a similar estimate and obtained a comparable result of 1.8 ± 0.4 m s^{-1}. Arzeno et al. (2020) examined satellite altimetry data and came to a similar conclusion that the first two baroclinic modes are the main contributors to high-frequency mixed Rossby–gravity wave variability.

LF variability has a shorter vertical wavelength. Consistently, the projection of regressed LF meridional velocity shows large values at the fourth–sixth vertical modes (Fig. 10b). Again, the contributions from multiple modes result in the tendency for

vertical propagation of LF variability (Fig. 8h). We also estimated c from the dispersion relation of mixed Rossby–gravity waves and $k = -1.44 \times 10^{-6}$ m^{-1} obtained from coherence analysis, the result of which was 0.75 ± 0.07 m s^{-1} for $\omega = 0.05$ cpd. This is between the phase speed of the fourth and fifth vertical modes (0.80 and 0.66 m s^{-1}, respectively) and consistent with the results of the vertical mode projection.

The difference in the meridional width of variability shown in (Fig. 6) is related to the differences in vertical scale and the resulting c. The meridional length scale is written as $L_y = (c/\beta)^{1/2}$, where y denotes latitude; L_y is smaller if the associated vertical mode is higher and c is smaller. We calculated L_y from $N = 0.015$ s^{-1} and the estimated c. The results are 305 ± 5 km ($2.74° \pm 0.05°$) for HF variability and 181 ± 8 km ($1.63° \pm 0.08°$) for LF variability. For a free mixed Rossby–gravity wave, the meridional structure of meridional velocity is proportional to a Gaussian multiplied by a constant, $v_0 \exp[-y^2/(2L_y^2)]$. We fit the Gaussian to regressed meridional velocity (Fig. 6) along 80.5°E at day 0 by least squares and obtained $L_y = 279 \pm 15$ and 163 ± 7 km ($2.51° \pm 0.13°$ and $1.47° \pm 0.06°$) for HF and LF

TABLE 1. Mixed Rossby–gravity wave parameter values estimated for the HF band (0.06–0.1 cpd; 10–17 days in period) and the LF band (0.04–0.06 cpd; 17–25 days in period).

| Frequency band	HF band	LF band
Zonal phase speed	From −3.6 to −3.9 m s^{-1}	From −2.6 to −2.9 m s^{-1}
Zonal wavelength	5242 ± 368 km	4364 ± 1335 km
Vertical wavelength	1053 ± 313 m	297 ± 32 m
c from the dispersion relationship	2.13 ± 0.07 m s^{-1}	0.75 ± 0.07 m s^{-1}
Meridional length scale obtained from $L_y = (c/\beta)^{1/2}$	305 ± 5 km ($2.74° \pm 0.05°$)	181 ± 8 km ($1.63° \pm 0.08°$)
Meridional length scale obtained from Gaussian function fitting to v	279 ± 15 km ($2.51° \pm 0.13°$)	163 ± 7 km ($1.47° \pm 0.06°$)
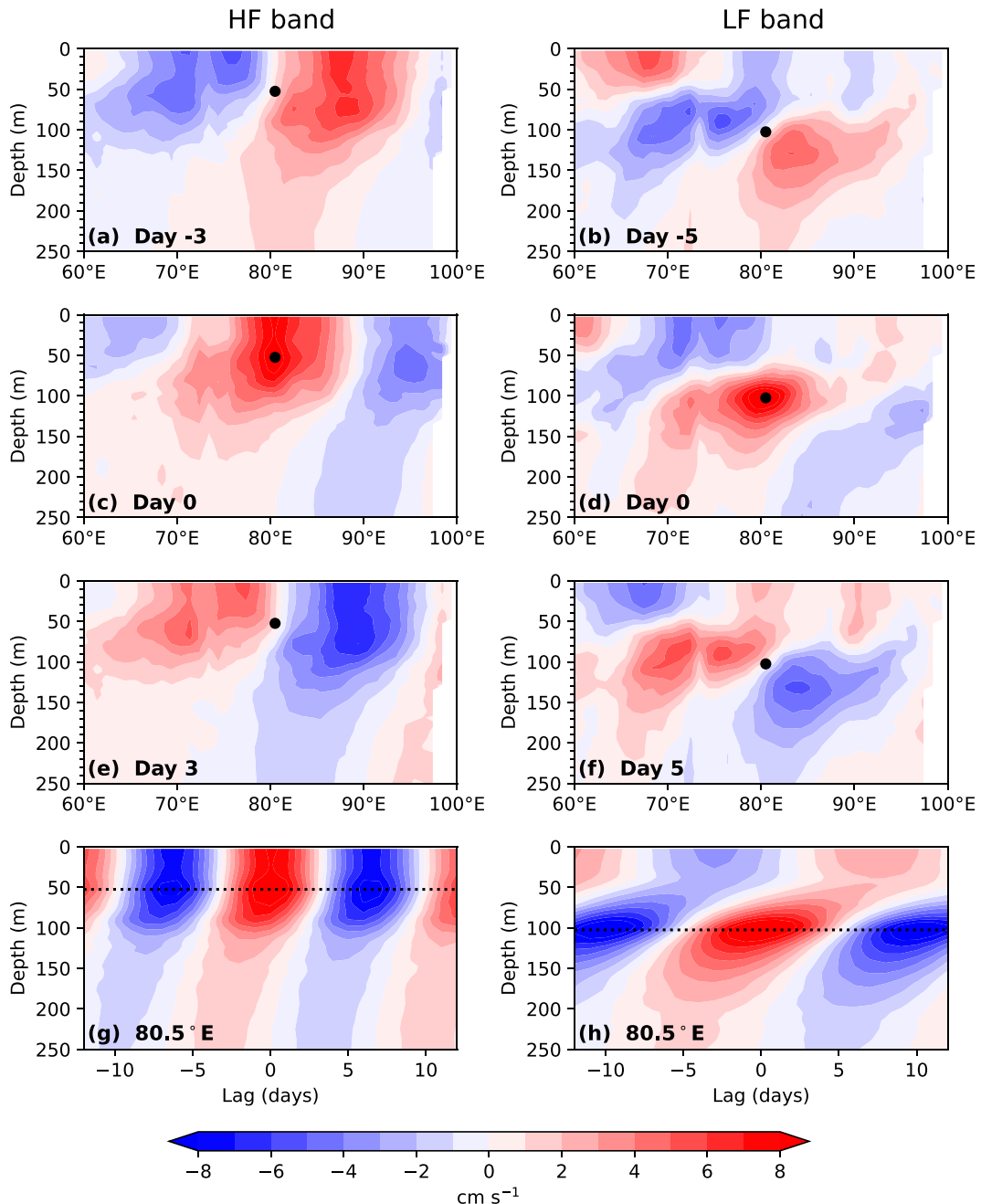
FIG. 8. (a)–(f) Longitude-depth sections of regressed meridional velocity along the equator for (left) HF (0.06–0.1 cpd; 10–17 days in period) and (right) LF (0.04–0.06 cpd; 17–25 days in period) variability. Meridional velocity at 0°, 80.5°E is regressed onto HF meridional velocity time series at 52.5-m depthin (a), (c), and (e) and LF meridional velocity time series at 102.5-m depth in (b), (d), and (f). The location of the index time series is shown by the black dots. Also shown are depth–time sections of (g) HF variability in meridional velocity at 0°, 80.5°E regressed onto the time series at 52.5-m depth and (h) LF variability regressed onto the time series at 102.5-m depth. The depth of the index time series is shown by the dotted lines in (g) and (h).

variability, respectively. The uncertainty of these estimates was obtained from the Bootstrap method. These estimates roughly agree with those obtained from $L_y = (c/\beta)^{1/2}$.

We also computed zonal phase speed ω/k from the estimated zonal wavenumbers. The results are -4.85 ± 0.34 m s^{-1} for HF

variability and -2.53 ± 0.77 m s^{-1} for LF variability. The estimate for LF variability is consistent with that obtained from regression analysis (from -2.6 to -2.9 m s^{-1}), but that for HF variability is smaller than that from regression analysis (from -3.6 to -3.9 m s^{-1}). The mean zonal flow is eastward in the
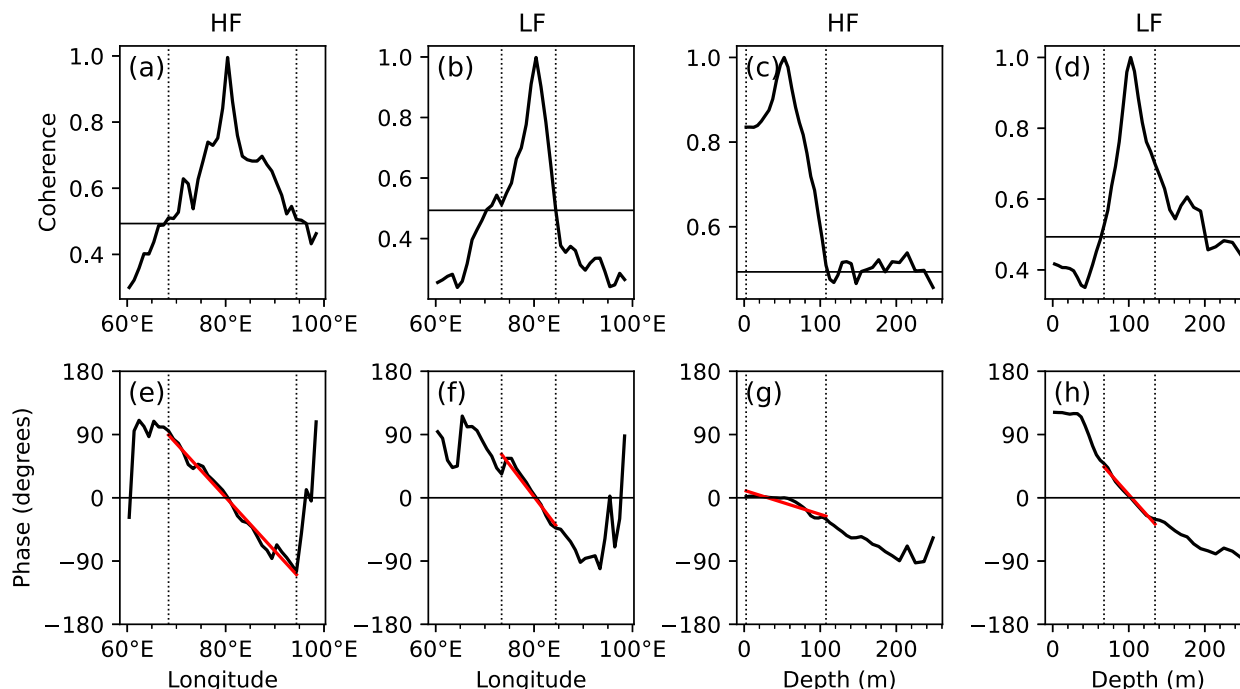
FIG. 9. (top) Coherence and (bottom) phase obtained from meridional velocity in the model control run, showing results (left),(left center) along the equator as a function of longitude and (right center),(right) at 0°, 80.5°E as a function of depth. Shown are (a),(c),(e),(g) HF variability and (b),(d),(f),(h) LF variability. An index time series at 52.5-m depth was used in (a) and (e), and one at 102.5-m depth was used in (b) and (f). Coherence and phase were computed with respect to the time series at 0°, 80.5°E and 52.5-m depth for HF variability and at 0°, 80.5°E and 102.5-m depth for LF variability. The solid horizontal lines in (a)–(d) illustrate the 99.5% confidence level for coherence. The vertical dotted lines show the region where a straight line was fit to the phase. The red lines in (e)–(h) are the regression slope fit to the phase using the linear least squares fit.

upper equatorial Indian Ocean (Nagura and McPhaden 2014), and its typical magnitude at 0°, 80.5°E is 0.1 m s^{-1} in our model. The Doppler shift (Arzeno et al. 2020; Smyth et al. 2015) does not account for the discrepancy between the phase speed for

HF variability estimated from the zonal wavenumber and regression analysis. It is unclear to us what accounts for this discrepancy, but the uncertainty in estimates of k and/or zonal phase speed is a likely possibility.
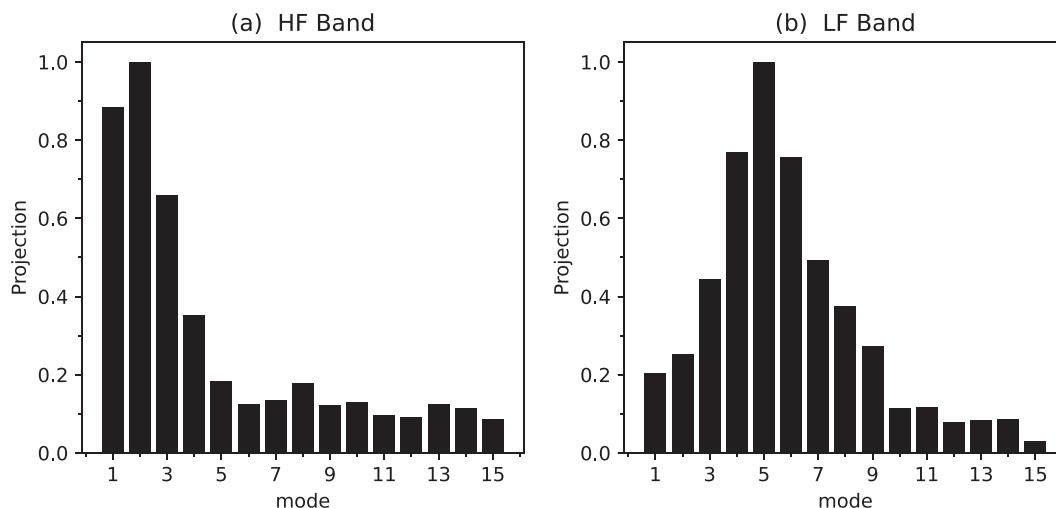

FIG. 10. Projection of regressed meridional velocity onto vertical modes computed from the mean stratification of the model for (a) HF and (b) LF variability. The projection was computed using regressed meridional velocity (shown in Fig. 8) at 0°, 80.5°E for two phases separated by approximately one-quarter of a cycle, i.e., days 0 and 3 for HF variability and days 0 and 5 for LF variability. The root-mean-square of the vertical mode amplitudes obtained from the two phases is shown. The results were normalized such that the maximum value is unity.

3) WIND FORCING

Previous studies pointed out that mixed Rossby–gravity waves in the central and eastern equatorial Indian Ocean are mainly excited by meridional winds (e.g., Arzeno et al. 2020; Miyama et al. 2006; PM21; Sengupta et al. 2004). Surface meridional wind stress shows elevated energy peaks west of about 60°E at frequencies of 0.03–0.1 cpd (10–33 days in period; Figs. 1b and 11). In the central and eastern basins, energy is highest east of 75°E in the HF band. An energy peak in the LF band is visible between 65° and 80°E, which is weak in magnitude but generates sizable variability in oceanic meridional velocity (section 3b).

Typically, the quasi-biweekly mode of atmospheric variability is defined as the variability at periods of 10–20 days, but previous studies used various definitions of the period range. For example, Chen and Chen (1995) used periods of 12–24 days; Kiladis and Wheeler (1995) used 6–30-day periods. Kikuchi and Wang (2009) suggested three definitions (12–20-, 10–20-, and 12–30-day periods) and reported that their results were not sensitive to the choice. It may be that LF variability in meridional wind stress at periods of 17–25 days is just the low-frequency tail of the quasi-biweekly mode. The horizontal structure of regressed surface wind stress shows that for our HF and LF definitions, variability has a similar clockwise circulation (Figs. 12a,b). This spatial structure of regressed surface wind stress is moreover robust against a slight change in the longitude of the index time series.

It is known that the quasi-biweekly mode propagates to the west (e.g., Kiladis and Wheeler 1995). Consistently, regressed meridional wind stresses on the equator propagate to the west in both the HF and LF bands (Figs. 12c,d). The zonal phase speed estimated by the Barron et al. (2009) method is −4.3 m s^{-1} for HF variability (with a range of uncertainty from −4.0 to −4.4 m s^{-1}) and −3.8 m s^{-1} for LF variability (with uncertainty from −3.5 to −4.1 m s^{-1}). These phase speeds are similar to those we estimated from meridional velocity (Table 1), suggesting that the ocean response is resonant with the wind forcing. This may explain why the sizeable amplitude of oceanic meridional velocity is excited by weak wind forcing in the LF band.

b. Numerical experiments

The spectra of meridional velocity obtained from the HF-TAU-CE experiment show elevated energy in the HF band (Fig. 13b), whose magnitude is weaker than but comparable to that in the control run (Fig. 13a). The spectral power in the LF band is negligible in the HF-TAU-CE experiment. In the LF-TAU-CE experiment, the spectral power is elevated in the LF band whereas that in the HF band is negligible (Fig. 13c). These results imply a linear response of meridional velocity variability at this location to wind forcing; that is, meridional velocity variability in the LF or HF band is driven by surface wind forcing in the same frequency band. The power in the LF-TAU-CE experiment is highest at about 100-m depth, which is consistent with the spectra obtained from the control run, indicating that surface wind forcing in the LF band is able to generate a subsurface energy peak. The highest
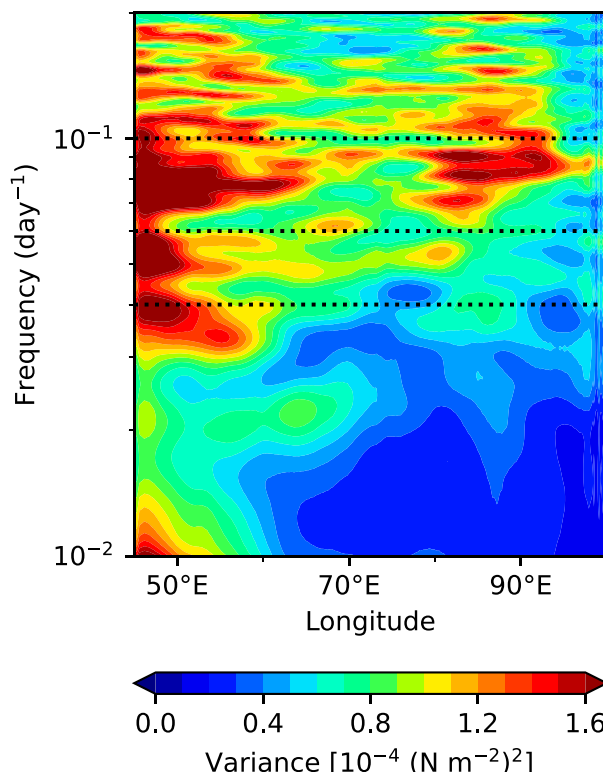

FIG. 11. Spectra of surface meridional wind stress averaged over 2°S–2°N as a function of longitude and frequency. Meridional wind stress was computed using the Large and Yeager (2004) bulk formula and JRA55-do surface winds. Frequencies of 0.04, 0.06, and 0.1 cpd (periods of 25, 17, and 10 days) are marked by dotted lines.

variance in the LF-TAU-CE experiment is also comparable to that in the control run.

The above results show the impact of wind forcing across the central and eastern basins. On the other hand, the variance of surface meridional wind stress is largest in the region west of 60°E (Fig. 11). To check the impact of wind forcing west of 60°E, the HF-TAU-W and LF-TAU-W experiments were conducted. The power of meridional velocity variability at 0°, 80.5°E is small in these experiments (Figs. 13d,e), showing the minor impact of wind forcing in the western basin. The variance of meridional velocity at 80.5°E is also small in the BACK-TAU experiment (Fig. 13f). David et al. (2011) proposed that the dynamical instability of the local currents contributes to the generation of LF variability in meridional velocity in the central equatorial Indian Ocean. Our results show that the contribution from local dynamical instability is minor. Also, this result shows that variability excited by dynamical instability in the western basin (Chatterjee et al. 2013; Kindle and Thompson 1989; Woodberry et al. 1989) does not reach the central basin, which is consistent with the results in Chatterjee et al. (2013) and Sengupta et al. (2001).

Figure 14 shows regressed meridional velocity along the equator obtained from the HF-TAU-CE and LF-TAU-CE experiments. The HF variability in the HF-TAU-CE experiment is surface trapped and slightly tilted upward toward the
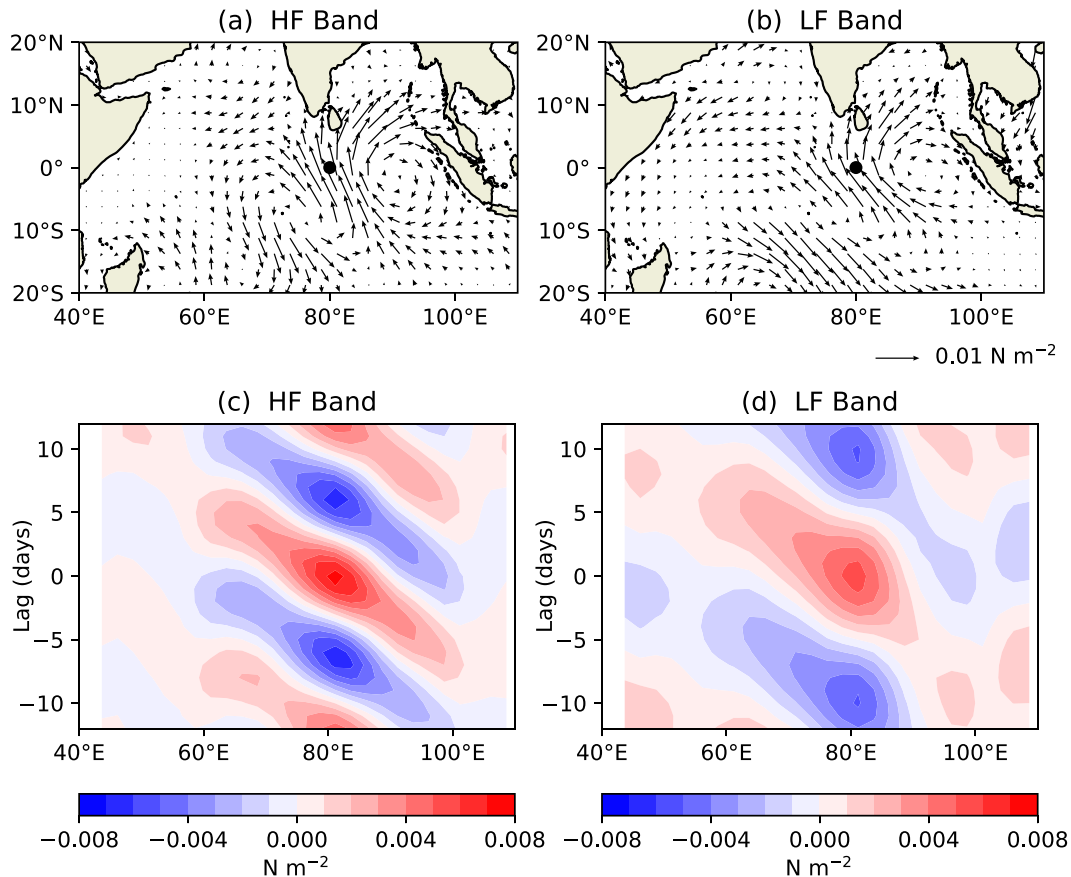
FIG. 12. (a),(b) Surface wind stress regressed onto meridional wind stress at 0°, 80°E. The index time series is normalized by its standard deviation. The filled circle marks the location of the index time series. Surface wind stress was computed using the Large and Yeager (2004) bulk formula and JRA55-do surface winds. (c),(d) Meridional wind stress along the equator regressed onto the same index time series as a function of time lag. Results are shown for (left) HF variability and (right) LF variability.

east below about 50-m depth (Figs. 14a,c,e), whereas LF variability in the LF-TAU-CE experiment is characterized by vertically stacked northward and southward velocities with a steeper upward tilt to the east (Figs. 14b,d,f). These structures resemble those in the control run (Fig. 8), indicating that variability in the HF-TAU-CE and LF-TAU-CE experiments is consistent with those in the control run.

Spectral power for the HF band obtained from the HF-TAU-CE experiment is large at the surface and east of about 80°E (Fig. 15a). This is the region where meridional wind stress has a large amplitude in the HF band (Fig. 11). The model is driven by HF wind stress in the region 10°S–10°N and 60°–110°E in the HF-TAU-CE experiment [section 2b(3)]. As a result, the variance of meridional velocity is small west of 70°E. The local peak of energy at about 50°E near the surface is a consequence of dynamical instability of the background current. Spectral power in the LF band obtained from the LF-TAU-CE experiment is large west of 70°E in the upper 130 m and east of 70°E at depths from 50 to 120 m (Fig. 15b). The subsurface peak of meridional velocity variance in the eastern basin is also seen in the control run (Fig. 5d). We suggest that

mixed Rossby–gravity waves generated at the surface propagate downward, then reflect and are trapped in the pycnocline at about 100-m depth, generating the energy peak there. Rothstein et al. (1985) pointed out similar trapping for an equatorial Kelvin wave. Note that the response to HF wind forcing is large east of 80°E (Fig. 15a), whereas that to LF wind forcing is seen mainly west of 90°E (Fig. 15b). The longitude where the ADCP was mounted, 80.5°E, is in the region where both HF and LF wind forcing is influential.

Intraseasonal winds in the western basin locally excite meridional velocity variations, but this energy does not reach the central and eastern basins. The large variance in the HF-TAU-W experiment is surface trapped and large in magnitude only west of 60°E (Fig. 15c). The large variance in the LF-TAU-W experiment extends to about 70°E in the upper 100 m but does not penetrate farther east (Fig. 15d). Also, variability excited by dynamical instability is confined to the region west of 65°E (Figs. 15e,f). The peak magnitude of meridional velocity variance west of 60°E is about 630 cm^2 s^{-2} in (Fig. 15b) and 544 cm^2 s^{-2} in (Fig. 15f), suggesting that dynamical instability generates LF variability in the western basin even in the absence
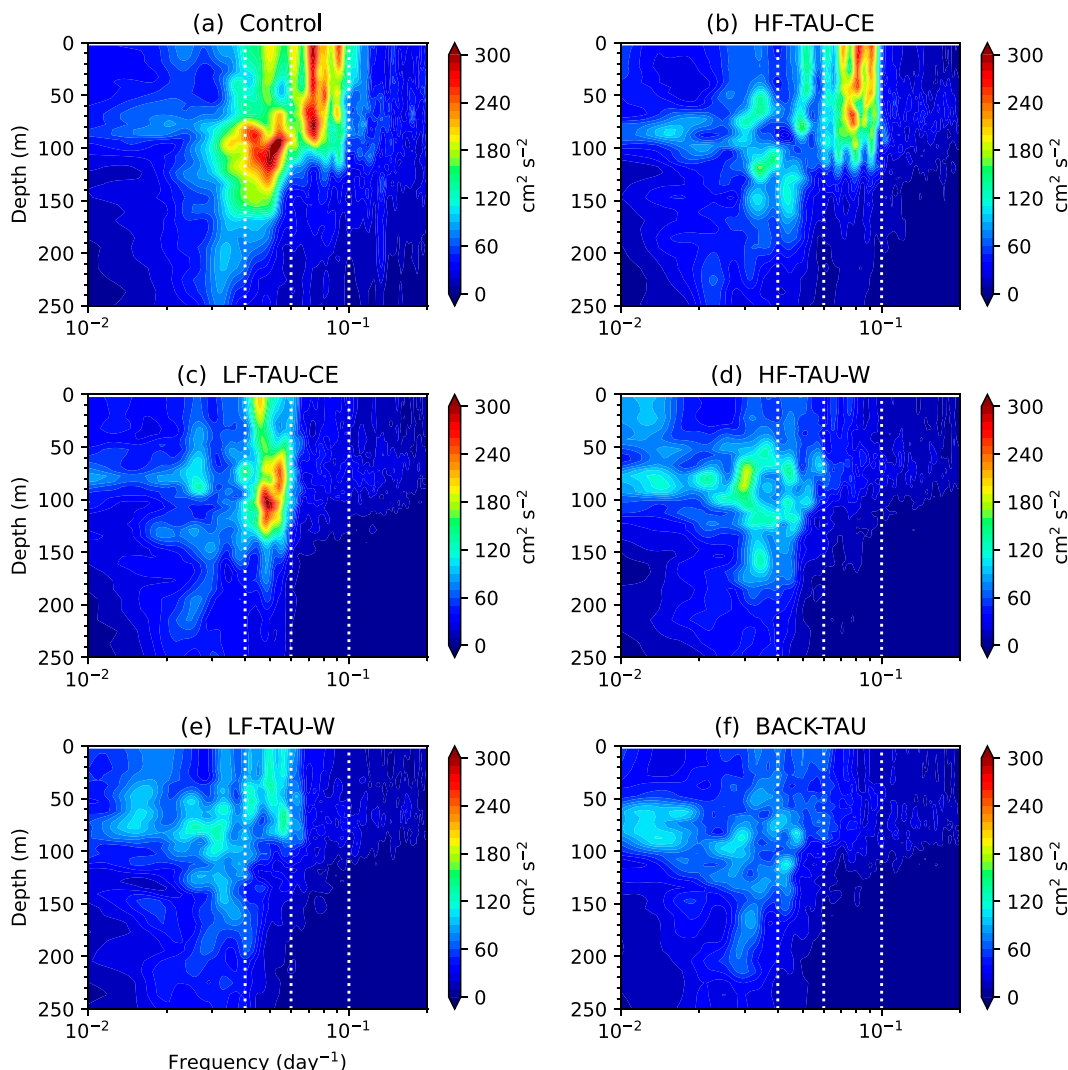
FIG. 13. Variance-preserving spectra of meridional velocity at 0°, 80.5°E as a function of frequency and depth obtained from (a) the control run and the sensitivity experiments (b) HF-TAU-CE, (c) LF-TAU-CE, (d) HF-TAU-W, (e) LF-TAU-W, and (f) BACK-TAU. The white dotted lines mark 0.04, 0.06, and 0.1 cpd (periods of 25, 17, and 10 days). Note that the color scale is the same as that in Figs. 2a and 2b.

of local wind forcing, as is reported by Chatterjee et al. (2013), Kindle and Thompson (1989), and Woodberry et al. (1989). The peak magnitude of meridional velocity variance in the western basin is about 700 cm² s⁻² in (Fig. 15d) and 770 cm² s⁻² in the control run (Fig. 5d), indicating that LF variability is further reinforced by local winds.

Miyama et al. (2006) used a linear, continuously stratified model with a flat bottom and reported that mixed Rossby–gravity waves excited in the western basin reach the eastern basin via bottom reflection. They also used an OGCM with realistic bottom topography and found that mixed Rossby–gravity wave energy propagating from the west is blocked by bottom topography near 75°E (likely the model Maldives) so it does not reach the eastern basin. To confirm this result, we removed the Maldives islands from our OGCM, flattened the ocean bottom by fixing it to a constant depth of 5100 m and

forced the model with the same surface wind stress as the HF-TAU-W experiment. Energy simulated in this experiment is elevated near the bottom at about 73°E (Fig. 16b) and near the surface at about 90°E (Fig. 16a), which is on the ray of a mixed Rossby–gravity wave. This result shows that energy excited in the western basin reaches the eastern basin via bottom reflections if the bottom is flat. The elevation of energy near the surface at about 90°E is absent in the HF-TAU-W experiment (Fig. 15c), which indicates that the rough topography hampers bottom reflections. We also confirmed that energy excited in the western basin does not reach the eastern basin when the ocean bottom is flattened but the Maldives islands are preserved, or when the Maldives islands are removed but the rough ocean bottom was kept. This result shows that either of the roughness of the ocean bottom or the Maldives islands suppresses bottom reflections.
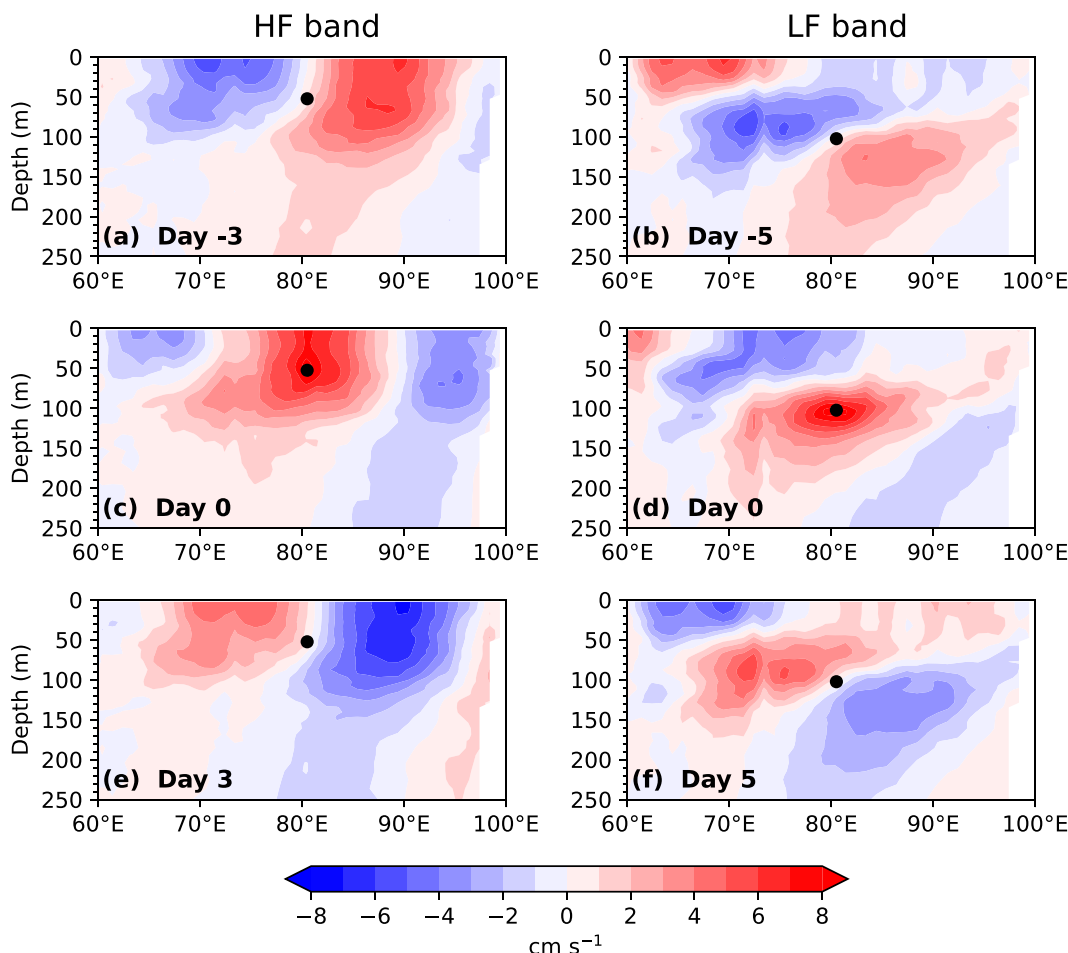
HF band

LF band

FIG. 14. Vertical structure of meridional velocity along the equator obtained from the HF-TAU-CE and LF-TAU-CE experiments: (a),(c),(e) HF variability regressed onto the time series at 0°, 80.5°E and 52.5-m depth. (b),(d),(f) As in (a), (c), and (e), but for LF variability regressed onto the time series at 0°, 80.5°E and 102.5-m depth. The location of the index time series for regression analysis is shown by the black dots.

4. Summary

Variability related to mixed Rossby–gravity waves in the Indian Ocean is often referred to as having "biweekly" periods (e.g., Miyama et al. 2006). However, in situ observations in the central equatorial Indian Ocean (0°, 80.5°E) show dual peaks in the spectrum of meridional velocity, one in an HF band (0.06–0.1 cpd; 10–17 days in period) with variance that peaks near the surface, the other in an LF band (0.04–0.06 cpd; 17–25 days in period) that peaks in the pycnocline. This study was motivated by the desire to understand this unusual frequency structure as a function of depth. We used empirical analysis and a wind-forced OGCM in the Indian Ocean domain validated with in situ velocity measurements to address this problem.

Results of statistical analysis show that velocity variability in the HF and LF bands has a similar horizontal structure. However, the wave pattern is meridionally narrower in the LF band than in the HF band and the vertical wavelength is shorter for LF variability than for HF variability. HF variability

is characterized by surface-trapped energy, as is pointed out by PM21, whereas LF variability exhibits alternating meridional currents with higher vertical wavenumber at depth. HF variability in meridional velocity along the equator has a large amplitude above 100 m depth, whereas LF variability is largest below the surface east of 70°E. We estimated the zonal and vertical wavelengths using coherence analysis and confirmed that wavelengths of both HF and LF variability are consistent with the dispersion relation of mixed Rossby–gravity waves in an ocean at rest.

We conducted sensitivity experiments, in which the model was forced by HF and LF variability in surface wind stress. The results show that HF and LF variability in meridional velocity at the location of the ADCP mooring (0°, 80.5°E) is the response to wind forcing in the central and eastern Indian Ocean consistent with linear equatorial wave theory. The response to HF wind forcing is large in amplitude above the pycnocline, whereas that to LF wind forcing has a peak of energy at the depth of the pycnocline. It is likely that waves
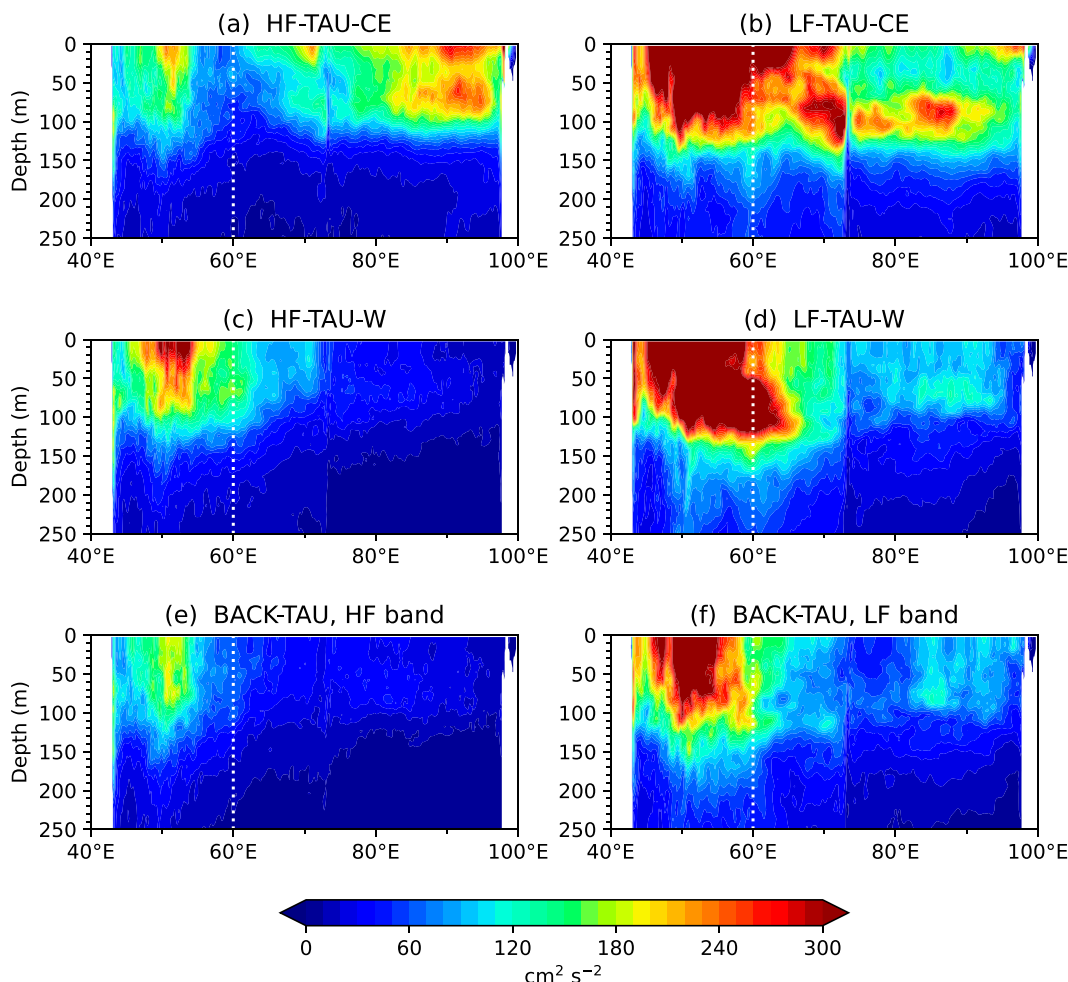
FIG. 15. Variance-preserving spectra of meridional velocity along the equator obtained from (a) the HF-TAU-CE experiment averaged over the HF band, (b) the LF-TAU-CE experiment averaged over the LF band, (c) the HF-TAU-W experiment averaged over the HF band, (d) the LF-TAU-W experiment averaged over the LF band, (e) the BACK-TAU experiment averaged over the HF band, and (f) the BACK-TAU experiment averaged over the LF band. The vertical dotted line marks the western edge of the CE region of the Indian Ocean (60°E). Note that the color scale is the same as that in Figs. 2a and 2b.

excited by LF winds propagate downward from the surface, reflect and are trapped in the pycnocline, generating the energy peak there. We conclude that this process creates the energy peak at the depth of the pycnocline in the LF band. The response to HF wind forcing is large in amplitude near the eastern boundary east of 80°E, whereas the response to LF wind forcing is largest in the central basin between 60° and 90°E. Wind forcing in the western basin near the African continent (west of 60°E) does not have a significant impact on meridional velocity variability in the central equatorial Indian Ocean, because the rough topography and the presence of the Maldives islands interfere with coherent bottom reflections and prevent energy excited in the western basin from reaching the eastern basin.

David et al. (2011) computed the baroclinic and barotropic conversion rate in the central equatorial Indian Ocean from satellite observations. They found that the energy conversion rate is large and positive in the years when the amplitude of

LF mixed Rossby–gravity waves is large. Then they hypothesized that local dynamical instability is the primary generator of mixed Rossby–gravity waves in the LF band in the central equatorial Indian Ocean. Whereas David et al. examined interannual variability in wave energy, we examine its temporal mean from 2008 to 2016 and found that wind forcing accounts for the energy of LF mixed Rossby–gravity waves (Fig. 13). As Chatterjee et al. (2013), Kindle and Thompson (1989), and Woodberry et al. (1989) pointed out, dynamical instability is the main driver of intraseasonal variability west of 60°E (Fig. 15). However, its contribution to energy in the central basin is negligible. It is still possible that local dynamical instability contributes to interannual variability in LF mixed Rossby–gravity waves to some extent, which should be investigated by numerical experiments in future work.

The above results show that mixed Rossby–gravity waves in the central Indian Ocean are composed of variability in two
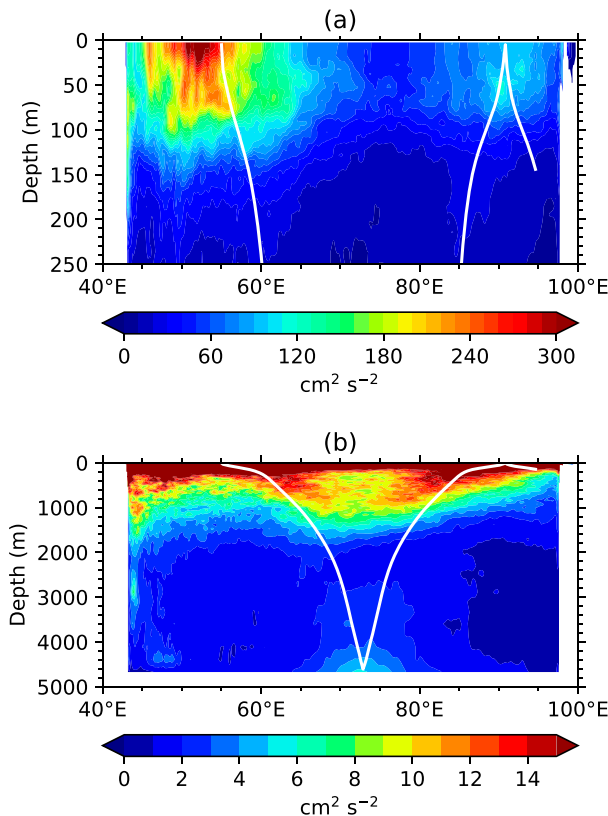
FIG. 16. Meridional velocity variance along the equator (a) in the upper 250 m and (b) in the whole water column obtained from the experiment in which the ocean bottom is flat and the model was driven by the same wind forcing as that in the HF-TAU-W experiment. The white line shows a mixed Rossby–gravity wave ray path computed from the Wentzel–Kramers–Brillouin method at the frequency of 0.07 cpd (about 14 days in period). Note that the color scale for (a) is the same as that in Figs. 2a and 2b.

distinct frequency bands, with different vertical wavelengths and meridional scales. Both of these waves are driven by surface winds, and their spatial structures are consistent with surface wind forcing at quasi-biweekly time scales. This knowledge can be a useful diagnostic tool for understanding the deep ocean response to atmospheric forcing. For example, Smyth et al. (2015) showed that the energy, heat fluxes, and the Stokes drift related to mixed Rossby–gravity waves are functions of wavelength and frequency. In a follow up study, we will assess how waves in the upper ocean detected by this study penetrate below the pycnocline and what impact they bring to the deep ocean.

APPENDIX

Methods of Statistical Analysis

This appendix summarizes our statistical method used in sections 3a(1) and 3a(2). We used the daily averages of zonal and meridional velocity obtained from the model, which are referred to here as $u(x, y, z, t)$ and $v(x, y, z, t)$, respectively. The variables x, y, z, and t are denoting the zonal, meridional, vertical, and temporal coordinates, respectively. We applied bandpass filtering to u and v and extracted HF and LF variability, which are u_{HF}, v_{HF}, u_{LF}, and v_{LF}. We used meridional velocity time series at 0°, 80.5°E as the index time series. This choice is owing to the fact that our model results are validated by the comparison with in situ observations at this location [section 2b(2)]. HF variability in meridional velocity is trapped in the upper 100 m, and the magnitude of LF variability peaks at about 100-m depth (Fig. 2b). Considering this, we used meridional velocity at 52.5-m depth as the index time series for HF variability and that at 102.5-m depth as that for LF variability. Note that 52.5 and 102.5 m are the depths at which the model grid points are located.

We computed regression coefficients using the filtered time series. The index time series is normalized by its standard deviation before regression analysis. HF variability, $u_{HF}(x, y, z, t)$ and $v_{HF}(x, y, z, t)$, is regressed onto $v_{HF\text{-norm}}(x = 80.5°E, y = 0°, z = -52.5\text{ m}, t = t - t_0)$, where the subscript "-norm" denotes that the time series is normalized, and t_0 is time lag. The time t spans the whole analysis period (16 August 2008–6 February 2016). Positive t_0 means that the target variable [$u_{HF}(x, y, z, t)$ or $v_{HF}(x, y, z, t)$] leads. The lag t_0 is from −12 to 12 days. This calculation provides regression coefficients as a function of x, y, z, and t_0. For LF variability, $u_{LF}(x, y, z, t)$ and $v_{LF}(x, y, z, t)$ are regressed onto $v_{LF\text{-norm}}(x = 80.5°E, y = 0°, z = -102.5\text{ m}, t = t - t_0)$. Coherence (Fig. 9) was computed between $v_{HF}(x, y = 0°, z, t)$ and $v_{HF}(x = 80.5°E, y = 0°, z = -52.5\text{ m}, t)$ or between $v_{LF}(x, y = 0°, z, t)$ and $v_{LF}(x = 80.5°E, y = 0°, z = -102.5\text{ m}, t)$.

Note that the results obtained from the abovementioned analysis depend on the choice of the index time series and decorrelation scales of variability. For example, regressed velocity has a peak amplitude and a clear structure near the longitude of the index (Fig. 7). This does not mean that the amplitude of variability is the largest there, as is evident from the energy depth sections (Figs. 5b,d).

We repeated the analysis using an index time series of meridional velocity at various longitudes and depths. The inferred structure was not overly sensitive to the choice of the index time series if meridional velocity in the central and eastern equatorial Indian Ocean (roughly from 70° to

90°E) was used as the index. We also confirmed that the structure was essentially the same if the index is located at depths where meridional velocity has sizable energy (0–100-m depths for HF variability and 80–150-m depths for LF variability).

We also repeated the estimates of zonal phase speed, zonal wavelength, and vertical wavelength using regression and coherence analysis with various index time series. The results were essentially the same if the index time series was obtained from meridional velocity in the central and eastern Indian Ocean at depths where meridional velocity has large enough variance.

REFERENCES

Adcroft, A., C. Hill, and J. Marshall, 1997: Representation of topography by shaved cells in a height coordinate ocean model. *Mon. Wea. Rev.*, **125**, 2293–2315, https://doi.org/10.1175/1520-0493(1997)125<2293:ROTBSC>2.0.CO;2.

Amante, C., and B. W. Eakins, 2009: ETOPO1 1 arc-minute global relief model: Procedures, data sources and analysis. NOAA Tech. Memo. NESDIS NGDC-24, 19 pp., https://www.ncei.noaa.gov/products/etopo-global-relief-model.

Arzeno, I. B., S. N. Giddings, G. Pawlak, and R. Pinkel, 2020: Generation of quasi-biweekly Yanai waves in the equatorial Indian Ocean. *Geophys. Res. Lett.*, **47**, e2020GL088915, https://doi.org/10.1029/2020GL088915.

Ascani, F., E. Firing, P. Dutrieux, J. P. McCreary, and A. Ishida, 2010: Deep equatorial ocean circulation induced by a forced-dissipated Yanai beam. *J. Phys. Oceanogr.*, **40**, 1118–1142, https://doi.org/10.1175/2010JPO4356.1.

Barron, C. N., A. B. Kara, and G. A. Jacobs, 2009: Objective estimates of westward Rossby wave and eddy propagation from sea surface height analyses. *J. Geophys. Res.*, **114**, C03013, https://doi.org/10.1029/2008JC005044.

Chatterjee, A., D. Shankar, J. P. McCreary Jr., and P. N. Vinayachandran, 2013: Yanai waves in the western equatorial Indian Ocean. *J. Geophys. Res. Oceans*, **118**, 1556–1570, https://doi.org/10.1002/jgrc.20121.

Chatterjee, P., and B. N. Goswami, 2004: Structure, genesis and scale selection of the tropical quasi-biweekly mode. *Quart. J. Roy. Meteor. Soc.*, **130**, 1171–1194, https://doi.org/10.1256/qj.03.133.

Chen, G., and Coauthors, 2020: Determination of spatiotemporal variability of the Indian equatorial intermediate current. *J. Phys. Oceanogr.*, **50**, 3095–3108, https://doi.org/10.1175/JPO-D-20-0042.1.

Chen, T.-C., and J.-M. Chen, 1993: The 10–20-day mode of the 1979 Indian monsoon: Its relation with the time variation of monsoon rainfall. *Mon. Wea. Rev.*, **121**, 2465–2482, https://doi.org/10.1175/1520-0493(1993)121<2465:TDMOTI>2.0.CO;2.

——, and ——, 1995: An observational study of the South China Sea monsoon during the 1979 summer: Onset and life cycle. *Mon. Wea. Rev.*, **123**, 2295–2318, https://doi.org/10.1175/1520-0493(1995)123<2295:AOSOTS>2.0.CO;2.

Dai, A., T. Qian, K. E. Trenberth, and J. D. Milliman, 2009: Changes in continental freshwater discharge from 1948 to 2004. *J. Climate*, **22**, 2773–2792, https://doi.org/10.1175/2008JCLI2592.1.

David, D. T., S. P. Kumar, P. Byju, M. S. S. Sarma, A. Suryanarayana, and V. S. N. Murty, 2011: Observational evidence of lower-frequency Yanai waves in the central equatorial Indian

Ocean. *J. Geophys. Res.*, **116**, C06009, https://doi.org/10.1029/2010JC006603.

Delorme, B. L., and L. N. Thomas, 2019: Abyssal mixing through critical reflection of equatorially trapped waves off smooth topography. *J. Phys. Oceanogr.*, **49**, 519–542, https://doi.org/10.1175/JPO-D-18-0197.1.

d'Orgeville, M., B. L. Hua, and H. Sasaki, 2007: Equatorial deep jets triggered by a large vertical scale variability within the western boundary layer. *J. Mar. Res.*, **65**, 1–25.

Han, W., J. P. McCreary Jr., D. L. T. Anderson, and A. J. Mariano, 1999: Dynamics of the eastern surface jets in the equatorial Indian Ocean. *J. Phys. Oceanogr.*, **29**, 2191–2209, https://doi.org/10.1175/1520-0485(1999)029<2191:DOTESJ>2.0.CO;2.

Holmes, R. M., J. N. Moum, and L. N. Thomas, 2016: Evidence for seafloor-intensified mixing by surface-generated equatorial waves. *Geophys. Res. Lett.*, **43**, 1202–1210, https://doi.org/10.1002/2015GL066472.

Hua, B. L., M. D'Orgeville, M. D. Fruman, C. Menesguen, R. Schopp, P. Klein, and H. Sasaki, 2008: Destabilization of mixed Rossby gravity waves and the formation of equatorial zonal jets. *J. Fluid Mech.*, **610**, 311–341, https://doi.org/10.1017/S0022112008002656.

Johnson, E. S., and M. J. McPhaden, 1993: Structure of intraseasonal Kelvin waves in the equatorial Pacific Ocean. *J. Phys. Oceanogr.*, **23**, 608–625, https://doi.org/10.1175/1520-0485(1993)023<0608:SOIKWI>2.0.CO;2.

Kikuchi, K., and B. Wang, 2009: Global perspective of the quasi-biweekly oscillation. *J. Climate*, **22**, 1340–1359, https://doi.org/10.1175/2008JCLI2368.1.

Kiladis, G. N., and M. Wheeler, 1995: Horizontal and vertical structure of observed tropospheric equatorial Rossby waves. *J. Geophys. Res.*, **100**, 22 981–22 997, https://doi.org/10.1029/95JD02415.

Kindle, J. C., and J. D. Thompson, 1989: The 26- and 50-day oscillations in the western Indian Ocean: Model results. *J. Geophys. Res.*, **94**, 4721–4736, https://doi.org/10.1029/JC094iC04p04721.

Krishnamurti, T. N., and P. Ardanuy, 1980: The 10 to 20-day westward propagating mode and "breaks in the monsoons." *Tellus*, **32A**, 15–26, https://doi.org/10.3402/tellusa.v32i1.10476.

Large, W. G., and S. Yeager, 2004: Diurnal to decadal global forcing for ocean and sea-ice models: The data sets and flux climatologies. NCAR Tech. Note NCAR/TN-460+STR, 112 pp., https://doi.org/10.5065/D6KK98Q6.

Locarnini, R. A., and Coauthors, 2013: *Temperature*. Vol. 1, *World Ocean Atlas 2013*, NOAA Atlas NESDIS 73, 40 pp., http://data.nodc.noaa.gov/woa/WOA13/DOC/woa13_vol1.pdf.

Masumoto, Y., and Coauthors, 2004: A fifty-year eddy-resolving simulation of the world ocean – Preliminary outcomes of OFES (OGCM for the Earth Simulator). *J. Earth Simul.*, **1**, 35–56, https://doi.org/10.32131/jes.1.35.

——, H. Hase, Y. Kuroda, H. Matsuura, and K. Takeuchi, 2005: Intraseasonal variability in the upper layer currents observed in the eastern equatorial Indian Ocean. *Geophys. Res. Lett.*, **32**, L02607, https://doi.org/10.1029/2004GL021896.

McCreary, J. P., 1984: Equatorial beams. *J. Mar. Res.*, **42**, 395–430.

McPhaden, M. J., and Coauthors, 2009: RAMA: The Research Moored Array for African–Asian–Australian Monsoon Analysis and Prediction. *Bull. Amer. Meteor. Soc.*, **90**, 459–480, https://doi.org/10.1175/2008BAMS2608.1.

——, Y. Wang, and M. Ravichandran, 2015: Volume transports of the Wyrtki jets and their relationship to the Indian Ocean dipole. *J. Geophys. Res. Oceans*, **120**, 5302–5317, https://doi.org/10.1002/2015JC010901.

Ménesguen, C., B.-L. Hua, M. D. Fruman, and R. Schopp, 2009: Dynamics of the combined extra-equatorial and equatorial deep jets in the Atlantic. *J. Mar. Res.*, **67**, 323–346, https://doi.org/10.1357/002224009789954766.

Miyama, T., J. P. McCreary Jr., D. Sengupta, and R. Senan, 2006: Dynamics of biweekly oscillations in the equatorial Indian Ocean. *J. Phys. Oceanogr.*, **36**, 827–846, https://doi.org/10.1175/JPO2897.1.

Nagura, M., and M. J. McPhaden, 2010: Wyrtki jet dynamics: Seasonal variability. *J. Geophys. Res.*, **115**, C07009, https://doi.org/10.1029/2009JC005922.

——, and ——, 2014: Zonal momentum budget along the equator in the Indian Ocean from a high-resolution ocean general circulation model. *J. Geophys. Res. Oceans*, **119**, 4444–4461, https://doi.org/10.1002/2014JC009895.

——, and Y. Masumoto, 2015: A wake due to the Maldives in the eastward Wyrtki jet. *J. Phys. Oceanogr.*, **45**, 1858–1876, https://doi.org/10.1175/JPO-D-14-0191.1.

——, ——, and T. Horii, 2014: Meridional heat advection due to mixed Rossby gravity waves in the equatorial Indian Ocean. *J. Phys. Oceanogr.*, **44**, 343–358, https://doi.org/10.1175/JPO-D-13-0141.1.

Noh, Y., and H. J. Kim, 1999: Simulations of temperature and turbulence structure of the oceanic boundary layer with the improved near-surface process. *J. Geophys. Res.*, **104**, 15621–15634, https://doi.org/10.1029/1999JC900068.

Ogata, T., H. Sasaki, V. S. N. Murty, M. S. S. Sarma, and Y. Masumoto, 2008: Intraseasonal meridional current variability in the eastern equatorial Indian Ocean. *J. Geophys. Res.*, **113**, C07037, https://doi.org/10.1029/2007JC004331.

——, M. Nagura, and Y. Masumoto, 2017: Mean subsurface upwelling induced by intraseasonal variability over the equatorial Indian Ocean. *J. Phys. Oceanogr.*, **47**, 1347–1365, https://doi.org/10.1175/JPO-D-16-0257.1.

Pacanowski, R. C., and S. M. Griffies, 2000: MOM 3.0 manual. NOAA/Geophysical Fluid Dynamics Laboratory Ocean Group Tech. Rep. 4, 682 pp., https://www.gfdl.noaa.gov/wp-content/uploads/files/model_development/ocean/mom3_manual.pdf.

Proehl, J. A., 1998: The role of meridional flow asymmetry in the dynamics of tropical instability. *J. Geophys. Res.*, **103**, 24597–24618, https://doi.org/10.1029/98JC02372.

Pujiana, K., and M. J. McPhaden, 2021: Biweekly mixed Rossby-gravity waves in the equatorial Indian Ocean. *J. Geophys. Res. Oceans*, **126**, e2020JC016840, https://doi.org/10.1029/2020JC016840.

Reppin, J., F. A. Schott, J. Fischer, and D. Quadfasel, 1999: Equatorial currents and transports in the upper central Indian Ocean: Annual cycle and interannual variability. *J. Geophys. Res.*, **104**, 15495–15514, https://doi.org/10.1029/1999JC900093.

Roemmich, D., and J. Gilson, 2009: The 2004–2008 mean and annual cycle of temperature, salinity, and steric height in the global ocean from the Argo Program. *Prog. Oceanogr.*, **82**, 81–100, https://doi.org/10.1016/j.pocean.2009.03.004.

Rothstein, L. M., D. W. Moore, and J. P. McCreary, 1985: Interior reflections of a periodically forced equatorial Kelvin wave. *J. Phys. Oceanogr.*, **15**, 985–996, https://doi.org/10.1175/1520-0485(1985)015<0985:IROAPF>2.0.CO;2.

Sasaki, H., and Coauthors, 2020: A global eddying hindcast ocean simulation with OFES2. *Geosci. Model Dev.*, **13**, 3319–3336, https://doi.org/10.5194/gmd-13-3319-2020.

Sengupta, D., R. Senan, and B. N. Goswami, 2001: Origin of intraseasonal variability of circulation in the tropical central Indian Ocean. *Geophys. Res. Lett.*, **28**, 1267–1270, https://doi.org/10.1029/2000GL012251.

——, ——, V. S. N. Murty, and V. Fernando, 2004: A biweekly mode in the equatorial Indian Ocean. *J. Geophys. Res.*, **109**, C10003, https://doi.org/10.1029/2004JC002329.

Smyth, W. D., T. S. Durland, and J. N. Moum, 2015: Energy and heat fluxes due to vertically propagating Yanai waves observed in the equatorial Indian Ocean. *J. Geophys. Res. Oceans*, **120**, 1–15, https://doi.org/10.1002/2014JC010152.

Strutton, P. G., V. J. Coles, R. R. Hood, R. J. Matear, M. J. McPhaden, and H. E. Phillips, 2015: Biogeochemical variability in the equatorial Indian Ocean during the monsoon transition. *Biogeoscience*, **12**, 2367–2382, https://doi.org/10.5194/bg-12-2367-2015.

Tsujino, H., and Coauthors, 2018: JRA-55 based surface dataset for driving ocean-sea-ice models (JRA55-do). *Ocean Modell.*, **130**, 79–139, https://doi.org/10.1016/j.ocemod.2018.07.002.

Wang, Y., M. J. McPhaden, P. Freitag, and C. Fey, 2015: Moored acoustic Doppler profiler time series in the central equatorial Indian Ocean. NOAA Tech. Memo. OAR-PMEL-146, 23 pp., https://www.pmel.noaa.gov/pubs/PDF/wang4307/wang4307.pdf.

Woodberry, K. E., M. E. Luther, and J. J. O'Brien, 1989: The wind-driven seasonal circulation in the southern tropical Indian Ocean. *J. Geophys. Res.*, **94**, 17985–18002, https://doi.org/10.1029/JC094iC12p17985.

Yoon, J.-H., 1981: Effects of islands on equatorial waves. *J. Geophys. Res.*, **86**, 10913–10920, https://doi.org/10.1029/JC086iC11p10913.

Zweng, M. M., and Coauthors, 2013: *Salinity*. Vol. 2, *World Ocean Atlas 2013*, NOAA Atlas NESDIS 74, 39 pp., https://repository.library.noaa.gov/view/noaa/14848.